Dottorato di Ricerca in Ingegneria dei Prodotti e dei Processi Industriali

Development of continuous flow microreactor for Buchwald-Hartwig amination

Analysis of reaction kinetics and microreactor clogging

Luca Sicignano

PhD in Industrial Product and Process Engineering - XXX Cycle

Dipartimento di Ingegneria Chimica, dei Materiali e
della Produzione Industriale
Università Federico II di Napoli

Tutor

Prof. Stefano Guido

Prof. Giovanna Tomaiuolo

2018

Success is not what you achieve in your life,
but what you inspire in the others

Contents

List of figures

Abbreviations

LFR	Laminar flow reactor
Re	Reynolds number
Pe	Péclet number
Pe_a	Axial Péclet number
Pe_r	Radial Péclet number
GCI	Green Chemistry Institute
DLVO	Derjaguin-Landau-Verwey-Overbeek
DLCA	Diffusion-limited cluster aggregation
RLCA	Reaction-limited cluster aggregation
CC	Cluster-cluster
PC	Particle-cluster
PP	Particle-particle
Br	Breakage number
T	Cluster cohesion force
B-H	Buchwald-Hartwig
SEM	Scanning Electron Microscope
XRD	Energy Dispersive X-ray
BF	Brightfield
CLSM	Confocal laser scanning microscopy
OD	Optical density
POM	Polarized optical microscopy
Np	Number of primary particles

Abstract

Several applications, ranging from petrochemical industry to pharmaceutical processes, involve the use of microfluidics devices in order to manipulate and study heterogeneous systems under flow in view of process intensification. These devices present many advantages, including lower flow rate compared to traditional batches, higher speed of heat and mass transfer, lower waste production and lower costs and operational safety. Otherwise, they show some drawbacks such as a lower degree of mixing, due to the laminar flow conditions typical of microfluidics, and solid formation, which may lead to the clogging of the device. For this reason, many studies are conducted to develop novel microsystems to combine the flexibility of batch reactors with all of the advantages of conventional flow systems and to understand the mechanisms basis to the solid handling, i.e. fouling problems.

Here, an innovative methodology to investigate the reaction kinetics of the Buchwald-Hartwig (B-H) cross-coupling reaction, chosen as key study, and the problem of solid handling in a continuous flow microreactor is presented. In particular, the first is investigated by developing a home-made microfluidic system to study the effects of process parameters, such as temperature and reagent concentration, on kinetic reaction, in order to optimize the microreactor set-up and the reactive process. Regarding the study of solid aggregation inside the device, it is examined by coupling microfluidic and microscopy and analyzing the effect of shear flow on surface fouling onto microchannel walls when running B-H reaction. To make this, a microfluidic apparatus has been created to process the reaction and to observe online aggregates growth and the subsequent clogging of the channels.

The present work is organized as follows: in Chapter 1, a general background about microreactors and solids handling, which causes the clogging problems, is presented by describing in detail the mechanisms at the base of surface fouling. In addition, the organic reaction of Buchwald-Hartwig run in the microreactor is described. Motivations of the study are also discussed. In Chapter 2, an innovative home-made flow

microreactor to process and to study B-H amination is presented. In particular, the efficiency of the microdevice is compared to the one of traditional batch reactors and a detailed study on the effect of the operating parameters is showed. In Chapter 3, the experimental set-up based on the microreactor is used as a novel approach to make the system more flexible in terms of number of feeds and imposed flow rates. Initially the results are compared to the previous ones to validate the new set-up. Subsequently, the effect of the operating parameters on the reaction kinetics are investigated to elaborate a kinetic law. In Chapter 4, the direct visualization of particles adhesion to the wall, cluster growth and reactor clogging is investigated in detail by using a home-made flow continuous device linked to a microfluidic system, in order to visualize the processes by microscopy techniques. In particular, the effect of the flow rate on cluster morphology and on channel clogging is analyzed, proposing an experimental alternative to study and understand the mechanism to the base of the surface fouling. Cluster formation and growth are studied by both qualitative and quantitative approach also using a mathematical model shown in the literature. Conclusions and future works are described in Chapter 5. Lastly in Appendix A shows the preparation protocol of the aryl bromide (i.e. the limiting reagent of B-H reaction), and in Appendix B reports in detail the home-made macro used to measure the cluster parameters, such as cluster area and cluster optical intensity of each image at different times.

1 Introduction

Micro-structured devices in continuous flow represent a key change for chemical industry, i.e. in manufacture of agrochemicals, petrochemicals and pharmaceuticals.[1-5] In this chapter, the microfluidic approach is presented as a viable alternative to classical batch reactor for developing "green" systems for chemical synthesis. Microreactors and fouling phenomena are described in detail. Finally, B-H cross-coupling reaction mechanisms are described, as well as the operating parameters influencing reaction kinetics.

1.1 Microreactors

A microreactor can be considered as a micro-device designed to run a chemical reaction in order to maximize the reaction performances minimizing size, costs, reagents and catalyst amount as well as safety problems (Figure 1.1)[6].

Figure 1.1 *The Model CFR-T consists of a 3/8-in.-diameter Type-316 stainless steel tube with mixing elements that divide the flow at the beginning of each element. Subsequent stretching and folding produces a radial motion of the high-velocity core regions outward toward the wall of the reactor, which has an inside diameter of about 0.20 in. (http://www.chemicalprocessing.com/articles/2006/tiny-reactors-aim-for-big-role)*

The microfluidic approach allows to run either the reactions that typically are not developed at small-scale, in order to have a pilot test for a further optimization of the process, or new reactive systems, also using renewable sources, i.e. light, sound, microwave, and ionic liquids.[7-12] Furthermore, the use of innovative devices ,allows a

reduction of work-up steps and the amount of materials for the reaction, leading to significant changes not only within industrial and technological sector (with the development of automated systems or of new process model) but also in the economy sector, developing new business models.[13-16] These factors have brought to the development of process intensification technologies based on microstructured devices, in which the process occurs at a dimension below 1 mm,[17] combining the advantages of continuous flow operation with those of microfluidics, such as the increase of surface-to-volume ratio compared to traditional systems, laminar flow, which is achieved by the combination of the characteristic dimensions at the micro-scale and the low flow velocities.[17-19] In addition, the confined flow conditions and the small internal volume of the reactor allow enhanced flexibility of operations (e.g. in terms of possible number of feeds)[20], ease of scaling-up[21], minimization of potential hazards, safety of operations at high process temperatures[22, 23] and low residence times[17]. The latter is very important for reactions with fast kinetics or for reactions which require particular conditions such as high temperature and mixing.[24]

Indeed, a microreactor is a laminar flow reactor (LFR) if the flow is fully developed, the flowing fluid is Newtonian, the velocity is determined at each point by its radial distance from the center of the tube only and the no-slip condition is valid, see Figure 1.2.

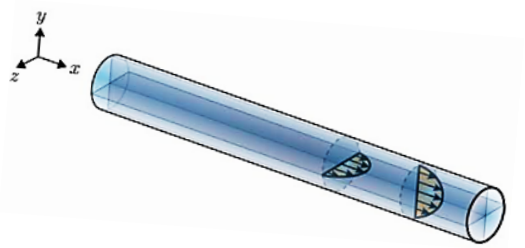

Figure 1.2 *Velocity profile in a tube.*[25]

The velocity profile is described by the following equation:

$$u = 2\bar{u}\left(1 - \left(\frac{r}{R}\right)^2\right) \qquad \textit{Equation 1}$$

where $\bar{u}$ is mean velocity, r is the generic position of the flow in the channel and R is the tube radius. To determine $\bar{u}$ is possible to couple Equation 1 with Hagen–Poiseuille law for cylindrical pipes. In fact, the Hagen-Poiseuille equation

$$\Delta P = \frac{8\mu L Q}{\pi R^4} \qquad \textit{Equation 2}$$

allows to determine the pressure drop ΔP in a channel for an incompressible and Newtonian fluid in laminar condition knowing the fluid viscosity μ, the flow rate Q, the channel length L and the channel radius R. In turn, knowing ΔP it is possible to determine the flow rate, which is directly proportional to the mean velocity $\bar{u}$

$$Q = \pi R^2 \bar{u} \qquad \textit{Equation 3}$$

where $\bar{u}$ is directly proportional with u_{MAX} which is the fluid velocity in centre of channel

$$\bar{u} = \frac{u_{MAX}}{2} \qquad \textit{Equation 4}$$

In general, it is possible to study the flow in the micro-channel by grouping the variables which control the system in two dimensionless parameters: Reynolds number and Péclet number.

The former, *Re,* is the ratio of inertial forces to viscous forces:

$$Re = \frac{\rho u D}{\mu} \qquad \textit{Equation 5}$$

where ρ is the fluid density, u is the velocity of the fluid, D is a characteristic dimension of channel (for a pipe D is the diameter) and μ is the dynamic viscosity of the fluid. Typical *Re* for microfluidic devices is lower than 2100 (laminar regime).

Péclet number, *Pe,* is the ratio of advection transport to diffusive transport and allows to evaluate the mixing in the channel for laminar condition.[25] Generally, *Pe* for microfluidic devices can range between 10-10^5 and is defined

$$Pe = \frac{uL}{k} \qquad \textit{Equation 6}$$

where u is the fluid velocity, k is the molecular diffusivity of the solute and L is a characteristic dimension of channel.[25] The latter variable depends on the Péclet number that is being evaluated, such as for the axial Péclet number Pe_a it is the channel length while for the radial Péclet number Pe_r the characteristic dimension is the channel radius.[26-28] By evaluating the interplay between two Péclet numbers, if the $Pe_r \gg 1$, (i.e. the radial diffusion is high), the solute goes towards channel walls, creating an asymmetric solute distribution which influences negatively both mixing and reaction kinetics. In addition, an increase of particle concentration near the microreactor walls can cause fouling problems (i.e. the unwanted deposition on surfaces) and consequently channel clogging.

In fact, a great drawback linked to the use of the micro-reactor, besides the low amount of final product (this problem can be overcome by numbering-up), is clogging due to fouling. Many organic reactions result in the generation of insoluble compounds, a reason that make difficult the synthesis of these reactions in microfluidic devices.[29] However, based on the studies performed in 2005 at Lonza Exclusive Synthesis[30] and at Green Chemistry Institute (GCI)[4], many organic reactions for pharmaceutical industry would benefit from the continuous approach (Figure 1.3) as the Buchwald-Hartwig amination reaction (see paragraph 1.3 Buchwald-Hartwig reaction).

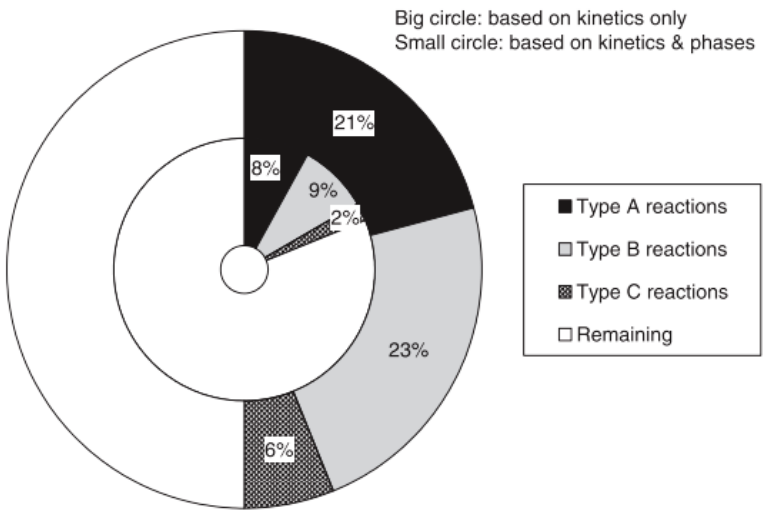

Figure 1.3 *According to our classification of eighty-six different reactions carried out Lonza, 50% would benefit from a continuous process (Type A, B and C), but 63% of those reactions cannot currently be carried out in a micro-reactor due to the presence of a solid.*[30]

However, until now the experimental studies on particle aggregation and clogging under microconfined conditions has been carried out on model systems, such as polymer-based colloidal suspensions, with a well-defined particle size and chemistry. Thus, the fluid dynamic behaviour of solids arising from chemical reaction, very pertinent with industrial applications, is still an open problem. Therefore, there is the need of a systematic quantitative investigation on fouling in micro-scale devices, allowing their further optimization.[30, 31]

1.2 Fouling and clogging

The undesired sedimentation and/or accumulation of suspended, dissolved or chemical generated solid material on clean solid surfaces is known as surface fouling. This phenomenon depends on the chemical nature of the substances and surfaces and on operating conditions, (i.e. temperature and flow field).[32] Surface fouling is ubiquitous in a broad range of industrial applications, such as chemical synthesis[33, 34], heat-transfer[35] and porous membrane-based water filtration.[36, 37] In fact, the particulate can clog the pores and/or the channels by causing a progressive flow rate reduction, until the entire

flow-channel cross-section gets blocked and the flow rate stops. A comprehensive overview on fouling was presented by Epstein et al. in 1983 through a 5x6 matrix where the five categories of surface fouling and the one particular type of clogging and the five events during the formation of fouling layers are reported (Figure 1.4).[38]

	1. Crystallization fouling	2. Particulate fouling	3. Chemical reaction fouling	4. Corrosion fouling	5. Biological fouling	6. Clogging by gas bubbles
Paper	**7**	**40**	**0**	**0**	**8**	**15**
Initiation [%]	43	35	0	0	75	60
Transport [%]	14	33	0	0	13	0
Attachment [%]	100	80	0	0	100	47
Removal [%]	29	43	0	0	13	80
Aging [%]	0	0	0	0	0	0

Figure 1.4 *5x6 Epstein matrix.*[38]

This matrix shows not only the fouling categories and the associated mechanisms but also the number of the scientific papers on each category, underlying the big effort made in this filed to understand fouling mechanism.

As shown in Figure 1.4, surface fouling can be distinguished in five events depending on the physical/chemical process at the base of fouling phenomena:

1. *Crystallization fouling* which can be caused by two events: i) precipitation of dissolved salts and fouling and ii) solidification of pure liquids or liquid mixtures due to freezing by sub-cooled surfaces.
2. *Particulate fouling* represents the sedimentation of solids initially present in the liquid phase.
3. *Chemical reaction fouling* is due to the formation of undesired insoluble substances in the bulk during the chemical reactions.

4. *Corrosion fouling* is caused by the deterioration of channel walls due to the surface heat transfer.
5. *Biological fouling* refers to the formation of bio-organisms on the surface during the production of biofilms.
6. *Clogging by gas bubbles* regards the presence of gas bubbles in the fluid owed to gas emissions during chemical reactions or degassing.[39]

Indeed, the sequence of mechanisms occurring in fouling processes can be summarized as (Figure 1.4):

i) *Initiation* indicates the delay time t_d needed to observe fouling onto a clean surface.
ii) *Transport* relates to the diffusion of particulate from the bulk phase to the surface.
iii) *Attachment* indicates the adhesion of solids onto the surface, except for the particulate fouling, in which the concentration at the surface C_s is taken equal to 0.
iv) *Removal* phase concerns the dislocation of the previously deposited layers on the surface due to shear flow and/or erosion and/or rupture caused by the flow. Sometimes this phase may also happen during the deposition phase.
v) *Aging* phase relates to the changes of the solid structure in a crystal morphology or a new chemical configuration.[40]

In detail, each phase previously described is governed by the particle-particle and particle-surface attractive/repulsive interactions and hydrodynamic forces, in turn dependent on flow regime[41], as shown in Figure 1.5.[42]

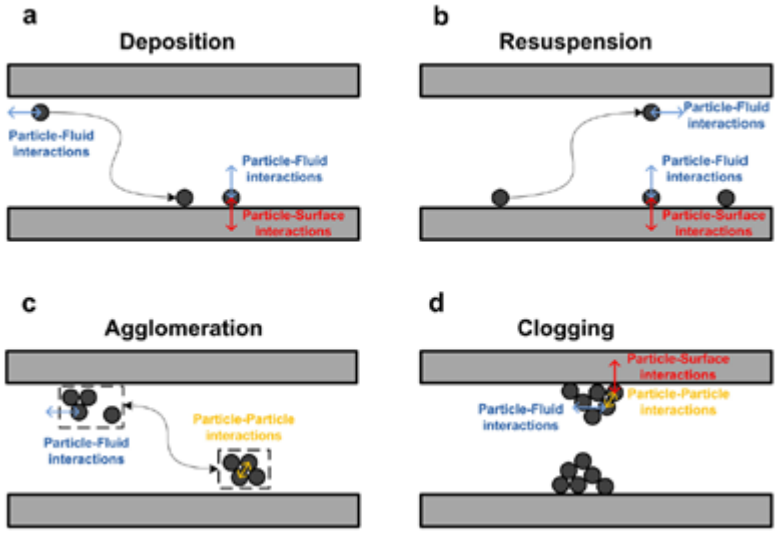

Figure 1.5 *Interactions governing the behaviour of solid particles in a microchannel: a) deposition; b) resuspension; c) agglomeration and d) clogging.*[42]

In Figure 1.5 four phenomena are showed: i) ***Deposition*** of particles on the microchannel walls due to the stronger particle-wall interactions compared to the particle-fluid interactions (Fig. 1.5a); ii) ***Resuspension*** in which the increase of flow rate breaks the particle-wall interactions and drags the particle, encouraging particle-fluid interaction (Fig. 1.5b); iii) ***Agglomeration*** of the suspended particles and dragged by flow due to particle-particle interactions by developing a cluster (Fig. 1.5c); iv) ***Clogging*** in which the cluster-wall interaction is higher than the cluster-fluid interaction, in addition the flow drags other particles by increasing the particle-particle and particle-cluster interactions blocking progressively the microchannel (Fig. 1.5d).[42] Obviously, the interactions differ case by case and depend on the chemistry and the morphology of the particles, the properties of the microchannel walls and the flow rate. The last event, clogging, is in turn governed by the previous three steps, and usually occurs via bridging of a constricted microchannel cross-section[29, 43] Bridging occurs when particles are growing in size reducing, initially, the flow rate and subsequently blocking the channel. Many studies have demonstrated that this phenomena are related not only to high particle volume fractions but also to flow rate and particle size, which must be 4:1 with the channel width.[44, 45]

Thanks to the great advantages offered by microfluidic devices, many studies have been focused on flow-induced particle aggregation in colloidal suspensions under microconfined conditions, to identify the parameters which influence this phenomenon, such as the effect of particle size[46, 47], shear rate[46-49] and volume fraction[48, 50-52]. In particular, for the latter some studies showed that surface fouling and subsequently channel clogging is faster for less volume fraction of large particles compared to more concentrated suspensions of small particles. This indicates a strong correlation between channel-height to particle-diameter ratio, contrarily to another study that accentuates an increase of the cluster growth with an increment of suspension volume fraction and velocity due to a rise of collision frequency. [48,49] In general, the main problem is that so far the few experimental studies on surface fouling have been carried out on model systems which does not allow to understand completely the phenomenon. However, a comprehensive overview of the above mentioned physical phenomena can be achieved by studying the three mechanisms of solids formation in flow reactor: i) *nucleation*, ii) *aggregation* and iii) *breakage*. In addition, a mathematical approach to understand the cluster growth and their morphology can be given using the *fractal theory*.

1.2.1 Nucleation

Nucleation is a process which involves in a preliminary formation of a phase nucleus in the bulk or on the channel surface which tends to increase over time. This mechanism is present in many processes, such as condensation, crystallization and evaporation and in industrial operation such as polymer production (i.e., nucleation and crystallization of bubbles[53]), biophysics (i.e., in the crystallization of proteins[54] and in virus replication[55]), and pharmaceutical synthesis[33, 56].

Nucleation can be homogeneous, when the nucleus is created by ions/molecules interactions already present in the bulk due to thermal fluctuation (this phase is known as self-nucleation)[57] or heterogeneous, when the nucleus starts its growth because there are impurities on surface of the channels which interact with the dragged particles in the bulk[58]. In both cases, the nucleation is a process energetically unfavourable because there is the need to provide energy to overcome the free energy barrier in order to form a new phase.

For homogeneous nucleation, the Gibbs free energy change ΔG can be expressed as the sum of two competitive factors: the volume free energy (negative value because it is released during change phase from liquid to solid) and the surface energy (positive value because the system absorbed it during the transformation)

$$\Delta G = -\frac{4}{3}\pi r^3 \left(\frac{\mu_L^0 - \mu_S^0}{V_M}\right) + 4\pi r^2 \sigma \qquad \textit{Equation 7}$$

where r is the radius of a primary solid particle formed from the liquid, μ_L^0 and μ_S^0 is respectively the chemical potential of the liquid and solid phase, V_M is the molar volume of the solid and σ is the interfacial tension.[39]

In view of this, by plotting the ΔG as a function of r can be observed that during the homogenous nucleation ΔG increases exponentially until a maximum, ΔG^*, which corresponds to the critical radius r^*, beyond which the free energy decrease quickly (Figure 1.6).[39] The ΔG^* and r^* value are expressed as

$$r^* = -\frac{2\sigma}{\left(\frac{\mu_L^0 - \mu_S^0}{V_M}\right)} \qquad \Delta G^* = \frac{16\pi\sigma^3}{3\left(\frac{\mu_L^0 - \mu_S^0}{V_M}\right)} \qquad \textit{Equation 8}$$

Therefore, ΔG^* represents the energy barrier that the aggregates must overcome in order that can form a nucleus, if not the cluster tends to crumble by stopping the growth.

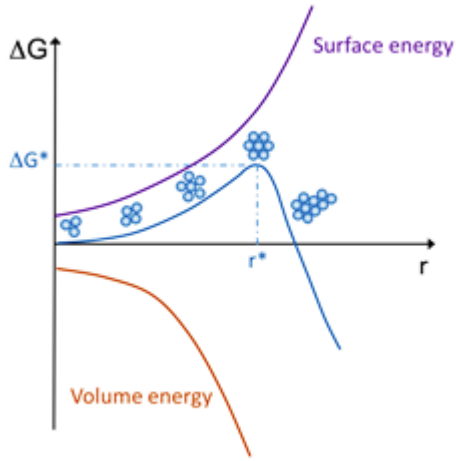

Figure 1.6 *Gibbs free energy as a function of nuclei radius.*[39]

Furthermore, many studies have showed the importance of the effect of the flow deformation on the nuclei. In fact, in this case, the hydrodynamic forces change the particle radius by causing an increase of ΔG^*, namely the particle growth can stopped for highest r and ΔG value compared to the stationary condition, Figure 1.7.[59]

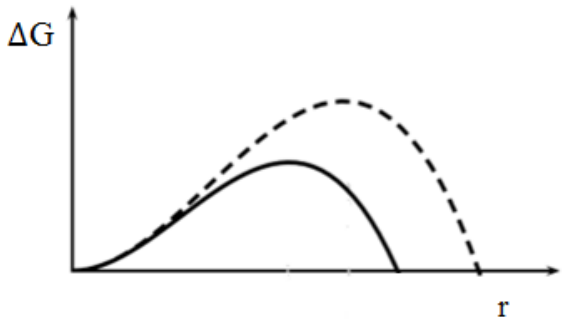

Figure 1.7 *Gibbs free energy as a function of particle radius. The continuous curve is in the absence of flow, while dashed curve is under shear conditions.*[59]

The effect shown in Figure 1.7 can be explained taking into account that the flow, in appropriate conditions, can counterintuitively facilitate the cluster growth because the frequency of particle collisions is increased.

Finally, Gibbs free energy for the homogenous nucleation can be expressed as

$$\Delta G = -\frac{4}{3}\pi r^3\left(\frac{\mu_L^0 - \mu_S^0}{V_M}\right) + 4\pi r^2 + \frac{1}{2}\frac{\eta\,\gamma}{G}\frac{4}{3}\pi r^3 \qquad \textit{Equation 9}$$

where η is the fluid viscosity, γ is the shear rate, G is the elastic deformation of the nucleus and the other parameters are previously described.[59]

For heterogeneous nucleation, the nucleus can form on the surface defects such as cracks, impurities, rough surfaces. Consequently, given that it needs a primer to cause the nucleation, the ΔG, in this case and in parity of the flow rate and chemical condition, is lower compared to homogenous nucleation because most of the nucleation energy is provided by the primer.[59]

1.2.2 Aggregation

Aggregation due to particle-particle and particle-surface interactions is a process that presumes an interplay between attractive and repulsive forces. These interactions are strongly influenced by surface roughness, particle size, shape and superficial charge. Many studies described this phenomenon by the Derjaguin-Landau-Verwey-Overbeek (DLVO) theory which asserts that the interactions depend on the combination of intermolecular van der Waals forces and electrostatic forces. For both, however, an energy reduction can be observed when the distance between the particles increases. In fact, plotting the two energetic contributions and the net interaction energy between particles as a function of the distance d between the particles it can be observed that a minimum energy value (energy barrier) has to be overcome to allow particle aggregation (Figure 1.8).[60]

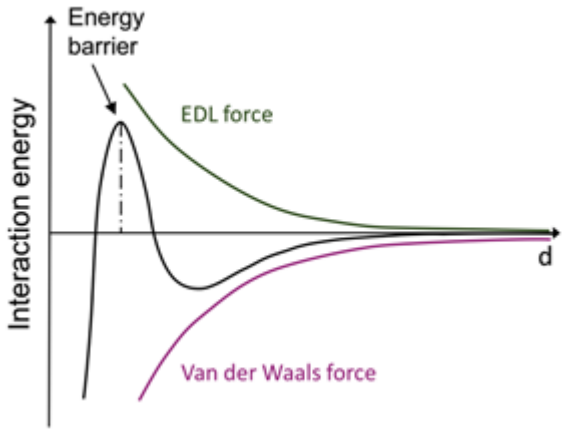

Figure 1.8 *Interaction energy between particles as a function of the distance between colloidal particles with the same z potential.*[60]

It is worth highlighting that, in the absence of repulsion forces, the particles which collide among them or with channel surface tend to aggregate instantly, this regime being called *diffusion-limited cluster aggregation* (DLCA). When repulsive forces are present, not all the collisions are effective, since not all of the particles can overcome the energy barrier (i.e. reaction-limited cluster aggregation (RLCA)).[61, 62]

Furthermore, in recent year DLVO theory for the aggregation kinetics has been extended to shear flow using an analytical solution to the governing diffusion-convection equation for two particles in the field of their intermolecular interactions.[63-66] This aspect is very important because the aggregation mechanism of DLVO particles in shear flows is very peculiar and different from any other aggregation mechanism: there is a competition between the flow convective transport and the DLVO energy barrier which leads to an abrupt increase of the aggregation rate as a function of Péclet as soon as the flow convection is able to overcome the barrier. As a result of this competition, the aggregation rate is initially slow and has a plateau equal to the Brownian reaction-limited rate and then explosively shoots up as soon as clusters are formed which have a Péclet number such that flow advection overcomes the DLVO barrier.[63-66]

Finally, DLVO theory allows to define when a colloidal system is stable, namely the aggregation velocity is not significant, or otherwise unstable when the rate of formation of aggregates is non-negligible and the number of the cluster-particle interactions increases. The latter phenomenon is known as flocculation and/or coagulation. In the literature, it is present a slight difference between these two events: the first indicates the formation of bigger structures called flocs, while the last refers to the aggregation of particles due to their collisions. In particular, depending on the collision, particle-cluster (PC) or cluster-cluster (CC), two different structures can be observed. In fact, in the case of particle-cluster collisions, the structures show a high radial symmetry, unlike the case of cluster-cluster interactions in which the structure is completely asymmetric, Figure 1.9.[67]

Figure 1.9 *Cluster-cluster (CC) and particle-cluster (PC) collisions.*[67]

In addition, CC interactions can be constructive or destructive depending on the particle size and the flow rate. In fact, constructive interactions occur when the clusters in the channel tend to grow not interacting with other cluster until the particles dragged by the flow fill the space among them creating a new great cluster, as shown in Figure 10.[52]

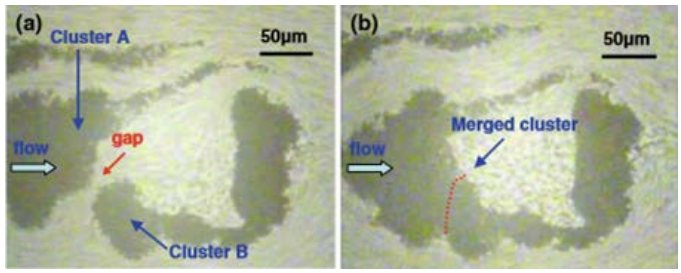

Figure 1.10 *Images depicting a constructive mode of CC interaction: (a) two clusters before merger and (b) a single cluster after merger.*[52]

Finally, destructive interactions occurs when a cluster dragged by the flow collides with a stationary cluster which is dragged away, Figure 1.11.[52]

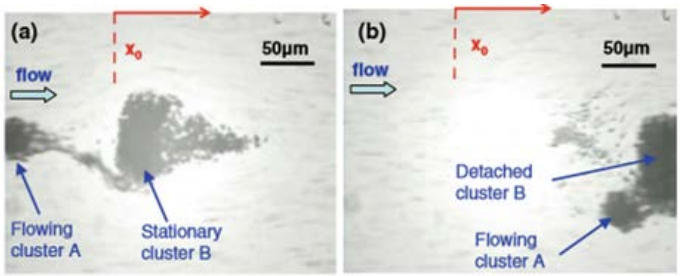

Figure 1.11 *Images depicting a destructive mode of cluster– cluster interaction: (a) a collision between a flowing particle aggregate and a stationary cluster and (b) cluster detachment following the collision.*[52]

1.2.3 Breakage

Breakage of cluster can occur when the aggregates tend to detach from the channel surface or when hydrodynamic forces erode the cluster surface. In fact, in the presence of the flow, the agglomerates can be subjected to two different forces, shear stress and tensile stress, causing two breakage mechanisms called *surface erosion* and *fragmentation* respectively (Figure 1.12).[39, 68] Surface erosion is governed by shear stress, which has a tangential action on the cluster surface beginning a slow detachment of small particles. The latter increases the probability of particle-particle (PP) and PC interactions. On the other hand, fragmentation is due to tensile forces, which act on the cluster normal direction, breaking agglomerates present in cluster of large dimensions.

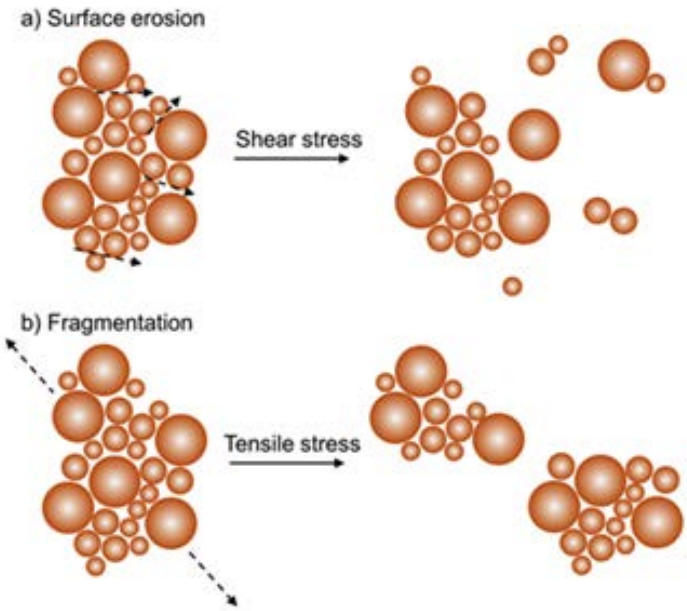

Figure 1.12 *Mechanism of cluster breakage: (a) surface erosion and (b) fragmentation.*[39]

Obvisuoly, each mechanism influeces cluster growth rate (R_{floc}) which results by an interplay between the collision rate (R_{col}) and the breakage rate (R_{br})

$$R_{floc} = \alpha R_{col} - R_{br} \qquad \textit{Equation 10}$$

where α is a collision efficiency coefficient or attachment coefficient which can be range between 0 and 1. This coefficient states the ratio between the successful collisions, carrying to PP interactions, over the total number of particle collisions. As seen above, the success of collisions depend on the overcoming of the energy barrier, therefore low α values coincide with a large energy barrier (i.e. stable colloidal system), while high α values corrispond to a low energy barrier (i.e unstable colloidal suspension).[69]

It is worth highlighting that the aggregation and breakage mechanisms can be described by two dimensions-less parameters, Péclet number (*Pe*) and Breakage number (*Br*). The first is largely described in the paragraph 1.1 on Microreactors (pg. 6) in which it has been seen that *Pe* is a gauge of the mixing in the channel for laminar condition because

it indicates an interplay between advection and diffusion forces. In this case, *Pe* allows to evaluate if the particle can interact and arrange among the others neatly or randomly. For high *Pe* values, the advection flow overbears the diffusive transport and the cluster structure is given by the collisions of the dragged particles, therefore the agglomerate structure is untidy. Contrariwise, for low *Pe* values, the diffusion predominates over the advection and the particles tend to organize neatly on cluster surface because the particles have all the time to arrange among them and to form clusters with neat and symmetrical structures.

Breakage number, *Br*, instead indicates the ratio between shear stress and cluster structural force

$$Br = \frac{\mu G R_P^3}{U_b} \qquad \textit{Equation 11}$$

where μ is the fluid viscosity, G is the shear rate, R_P is the particle radius and U_b is the cluster cohesion force.

U_b is an indication of agglomerate cohesion and the aptitude to resist to external forces, which tend to break the cluster. Therefore, for high *Br*, the hydrodynamic forces prevail on the cohesion ones, cluster breakage occurring, contrariwise for low *Br* values.[41, 70, 71] Considering this, many studies have showed the energy distribution of the forces in to the cluster subjected to flow in both the cases of cluster given by particle-cluster and cluster-cluster interactions.

For agglomerates derived from PC interactions (Figure 1.13a) the energy distribution is uniform, in fact the hydrodynamic force value is highest on the cluster surface compared to the one inside the cluster. This indicates of a strong cohesion of the particles in to the cluster. While, cluster due to CC interactions, the forces distribution is not uniform because the structure have not an uniform and symmetric configuration (Figure 1.13b).[67]

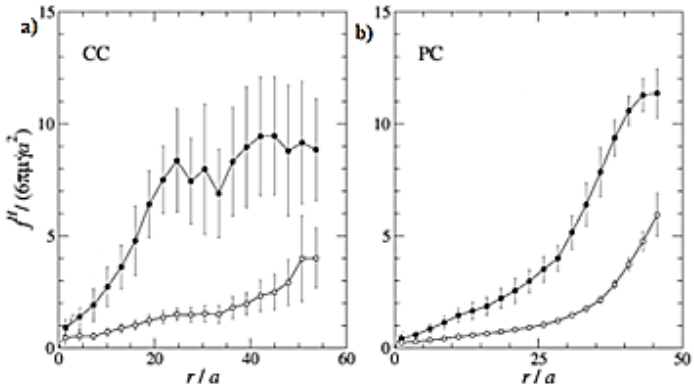

Figure 1.13 *Hydrodynamic force as a function of distance r from the center of mass for CC aggregates with Df =1.7, np=384 (left), and for PC aggregates with Df =2.3 and np = 800 (right).•, statistically expected maximum force; o, statistically expected average force.*[67]

1.2.4 Fractal theory

Fractal theory is a mathematical model which can be used when the aggregate shows a repetitive structure. Namely, a part of the cluster is identical to the entire cluster itself except smaller unit or primary agglomerate. This structure is called *fractal*. The fractal theory allows to understand how the primary aggregates tend to fill the spaces inside the volume occupied by the cluster.[72-75] An example of how cluster model can be analysed by using this theory is shown in Figure 1.14, in which it can be observed that the particles of small dimension (grey) arrange themselves creating a monotonous planar circular structure growing radially. Thus, the total mass of a cluster will vary for each agglomeration radius, namely will be directly proportional to the number of primary particles for cluster radius.[72, 76]

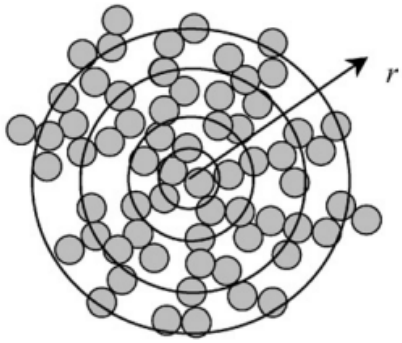

Figure 1.14 *Variation of cluster mass as a function of increasing radius.*[72]

In addition, it is possible to determine different fractal structures, depending on whether the agglomerate growth occurs along a single direction, or two or three. In these cases, the cluster structure is called linear or planar or volumetric, and the fractal dimensional is called one- or two- or three-dimensional, respectively, Figure 1.15.[72]

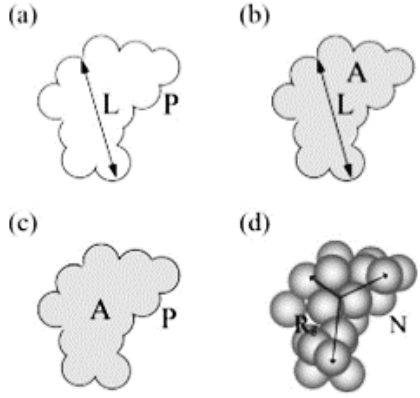

Figure 1.15 *Measurements of aggregate fractal dimensions. (a) One-dimensional fractal dimension power–law scaling with perimeter and the maximum length of an aggregate. (b) Two-dimensional fractal dimensions power–law scaling with area and the maximum length of an aggregate. (c) Perimeter- based fractal dimension power–law scaling with area and perimeter. (d) Three-dimensional fractal dimensions power–law scaling with the number of primary particles and the radius of gyration.*[76]

In literature, there many equations which allow to determine the fractal dimension for each configuration:

- One-dimensional D_1 can be given by the combination between the perimeter, *P*, and the mean length of the cluster, *L*

$$P = L^{D_1} \qquad \textit{Equation 12}$$

- Two-dimensional D_2 can be obtained by the connection between the size of the cluster, *A*, and *L (Equation 13a)*[72] or between *A* and *P* where d_{pf} is the perimeter fractal dimension *(Equation 13b)*[77]

$$A = L^{D_2} \qquad \textit{Equation 13a}$$

$$D_2 = \frac{2}{d_{pf}} \qquad A = P^{\frac{2}{d_{pf}}} \qquad \textit{Equation 13b}$$

- Three-dimensional D_3 can be got by the exponential association with D_2 *(Equation 14a)* or the linear equation with d_{pf} *(Equation 14b)*[76]

$$D_3 = 1.391 + 0.001e^{2.164D_2} \qquad \textit{Equation 14a}$$

$$D_3 = -1.628 + 4.6d_{pf} \qquad \textit{Equation 14b}$$

In addition, it is possible to determine the number of primary particle into the cluster, N, as a function of the fractal dimension, d_f

$$N = k\left(\frac{R_g}{a_P}\right)^{d_f} \qquad \textit{Equation 15}$$

where d_f is the fractal dimension which can range between 1 – 3 if the fractal is linear or spherical respectively, a_P is the radius of the primary particle, k is a prefactor can be a function of d_f and R_g is the radius of the gyration, which indicates that the particles are distributed around the rotation axis of the cluster. The latter, for spherical aggregates, is a function of the cluster radius, R

$$\frac{R}{R_g} = \sqrt{\frac{2 + d_f}{d_f}} \qquad \textit{Equation 16}$$

In literature, many studies have been conducted to determine the prefactor k which can range between 1 – 1.2 and can be expressed in the following equation[77]

$$k = 4.46 d_f^{-2.08} \qquad \textit{Equation 17}$$

Finally, the fractal dimension is an index of the particles aggregation. In fact, for equal number of primary particles, an increase of d_f coincides with a more compact cluster structure namely the agglomerates interactions are stronger compared to cluster with a low d_f in which the structure is open, Figure 1.16.[77]

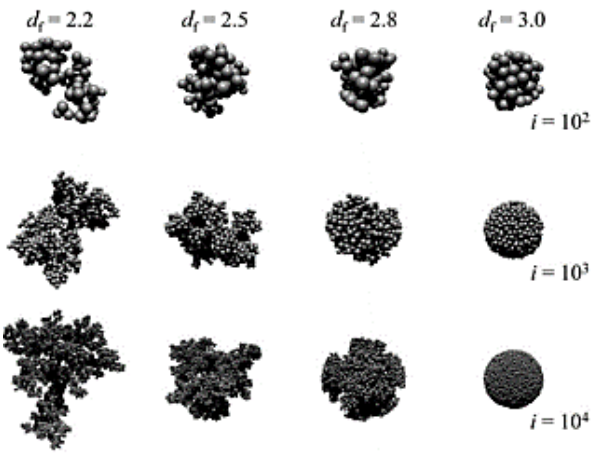

Figure 1.16 *Examples of aggregates obtained with the tuneable fractal dimension code and the densification via Voronoi tessellation.*[77]

1.3 Buchwald-Hartwig reaction

Buchwald-Hartwig (B-H) amination reaction is one of the most efficient cross-coupling reaction to prepare aryl amines.[78-80] This reaction is manly studied in the pharmaceutical field, for the production of drugs for the treatment of psycho-physical disorders[81] and in the agrochemical field, for the production of electronic materials and pigments.[82] This reaction, unlike other cross-coupling reactions, offers a lower reaction temperature, higher selectivity and does not utilize reagents that can cause safety problems.[83] B-H reaction discovered in 1994[84, 85] involves the coupling of an aryl halide and a primary or secondary amine in the presence of a palladium-based catalyst and a strong base, generally a alkali salt for the formation of an aromatic amine according to a reaction mechanisms in three steps, Figure 1.17.[19, 86, 87] The first step is the oxidative addition of the aromatic halide to palladium, which ends with the formation of Pd-halide complex. In the second step, the presence of the base results in two effects, the deprotonation of amine and the association of complex Pd-halide with amine which forms the new complex Pd-halide-amine. In the last step, there is the reduction of the complex Pd-halide-amine which returns the Pd to its initial state and releases the aromatic amine.

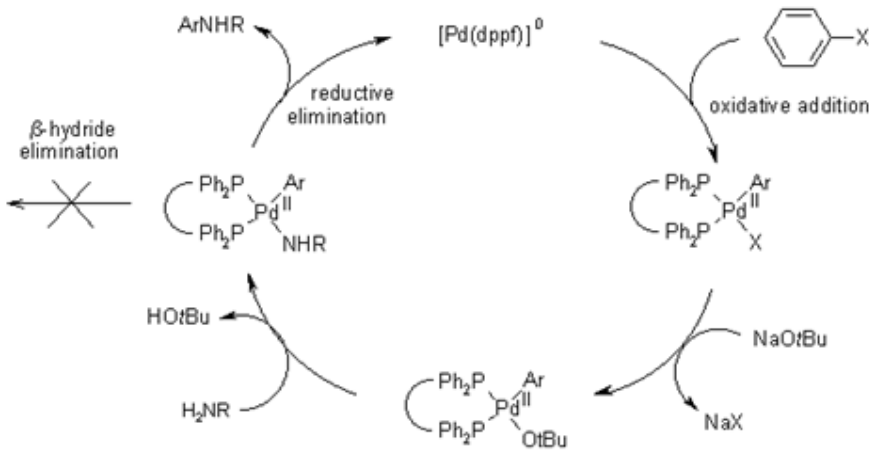

Figure 1.17 *Mechanism of the Buchwald-Hartwig Coupling. (http://www.organic-chemistry.org/namedreactions/buchwald-hartwig-reaction.shtm)*

Many studies state that the limited stage of the reaction is the oxidative addiction, for which the equation rate proposed in the literature is:

$$-\frac{d[ArBr]}{dt} = \frac{k_1 k_2}{k_{-1}[L]}[ArBr][Pd] \qquad \textit{Equation 18}$$

where $[ArBr]$, $[Pd]$ and $[L]$ are aryl bromide, palladium catalyst and ligand concentrations respectively, and k_1, k_2 and k_{-1} are the kinetic rate constants.[87]

It is worth highlighting that Equation 18 is related to a B-H reaction conducted with a catalyst consisting of a ligand (an organic component that accelerates the kinetic of the catalytic reaction) and palladium. In this case, it can be observed a direct linear first-order dependence on aryl halide and palladium concentrations, an inverse first-order dependence on ligand concentration and a zero-order dependence on amine concentration. Recent studies conducted by Pommella et al.[19] have shown that the choice of the palladium catalyst is of crucial importance for the performance of the reaction. In fact, using a particular Pd-catalyst without the ligand, the reaction exhibits better results in terms of yield and low catalyst concentration.[19]

In general, Buchwald-Hartwig reaction is influenced by operating parameters, such as temperature, concentration of catalyst, base and solvent, and by process parameters, as the choice of the appropriate reactor (batch or continuous flow). While the operating parameters are widely studied and schematized by Surry et al. in 2011[86], Figure 1.18, few studies has been conducted on the use of continuous flow configurations, despite the number of advantages, such as increase flexibility, lower catalyst concentration (namely low costs) and safety, compared to batch reactor.[19, 20]

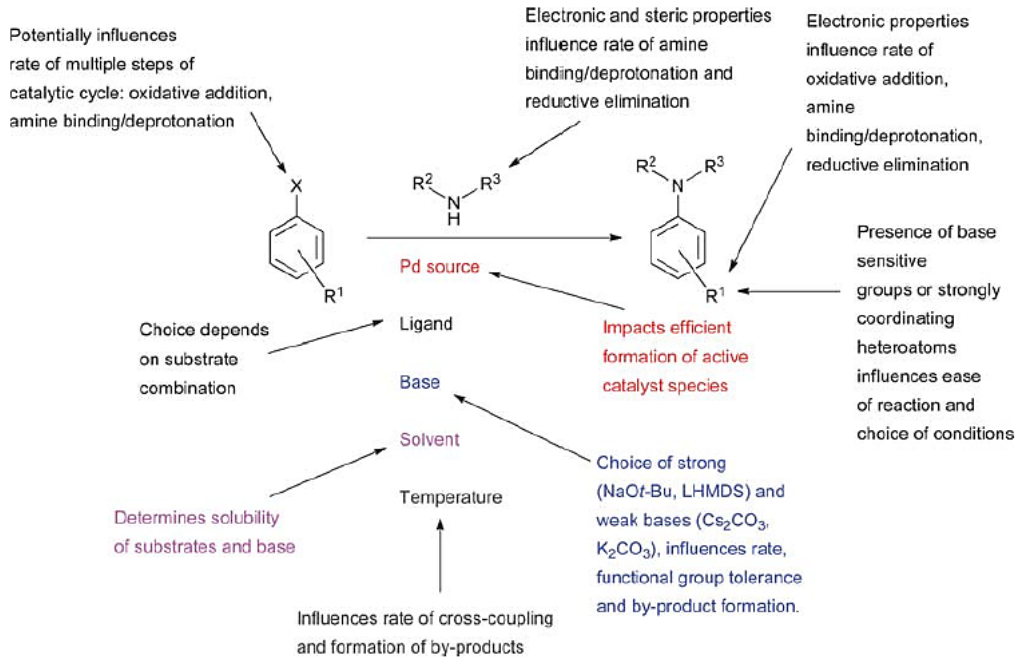

Figure 1.18 *Factors influencing the outcome of a Pd-catalyzed amination reaction.*[86]

The main difficult associated with running B-H reaction in a continuous flow reactor, especially in micro-scale systems, is the formation of potassium bromide (KBr) as by-product, a solid salt resulting from the use of an alkali metal alkoxide base and the aryl bromide, completely insoluble in toluene (the main solvent used for this reaction). The presence of this solid leads to the formation of suspended salt particles/clusters and a progressive denser slurry which clogs the microreactor, Figure 1.19.[39]

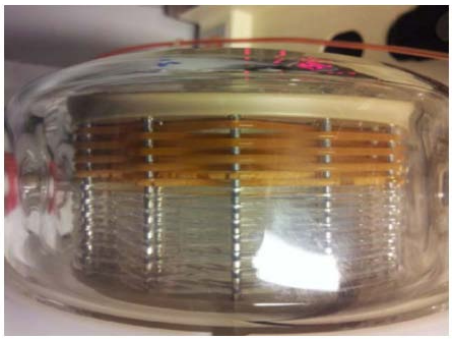

Figure 1.19 *An image of a PFA tubular reactor with forming inorganic salt, captured during continuous flow catalytic Buchwald–Hartwig amination reaction. The reaction was performed in a 10ml total volume PFA coil reactor by Vapourtec, with ID=1mm at flowrate of 1ml/min.*[39]

From Figure 1.19 it can be seen that the salt film covers uniformly the internal surface of the reactor from the inlet of the channel, becoming gradually less prominent. This phenomenon occurs via two parallel mechanisms: fouling on reactor surfaces due to wall nucleation, and formation of aggregates via bulk nucleation.[29] In this case, the formation and the growth of a KBr salt film is due to wall fouling, which blocks the flow path, while the nucleation in the bulk leads to the formation of suspended salt clusters, which further participate in hydrodynamic bridging (the contact between suspended salt agglomerates decreases gradually the flow path until clog the channel). Many solutions have been proposed in the literature for decreasing fouling, such as the increase of wall shear stress by increasing fluid velocity thus reducing particle-wall contacts, or the use of two-phase flow, allowing the introduction of a secondary phase which dissolves the solid particles or by using ultrasound.[88-91] All these solutions, however, are not applicable to all the types of clogging and furthermore they do not consider all real reasons for which the KBr cluster tend to aggregate and to interact with the microreactor walls.

1.4 Aim of the work

The need of a complete comprehension of solid handling in continuous flow microreactors for organic reaction is the main motivation of the present work. In the light of this, the aim of this work is to propose an innovative method to investigate the Buckwald-Hartwig amination reaction and the ensuing kinetics of undesired clusters aggregation by coupling microfluidics and microscopy techniques.

To this aim, a flexible and efficient flow microreactors have been developed with a configuration optimised to avoid clogging and to analyse the effect of the operating parameters, such as flow rate, temperature and catalyst concentration on reaction kinetics and surface fouling. In particular, it has been highlighted the influence of the flow rate on the aggregation process. In fact, by exploiting both image analysis and mathematical models related to fractal theory, the effect of flow field on KBr cluster morphology, size and growth rate has been investigated in detail.

This project of thesis, therefore, aspires to set the basis for an innovative experimental set-up that will be able to elucidate the mechanism at the base of solid aggregation in some continuous flow microsystems.

2 Microreactor in continuous flow for cross-coupling reactions

In this chapter, the continuous flow microreactor is presented as a valid tool for processing B-H cross-coupling reactions, and compared to batch reactors. Major attention is paid on the effects of operating parameters on B-H reaction kinetics. Experiments are carried out by using a stainless-steel tubular microreactor and a gas-chromatography coupled to mass spectroscopy (GC-MS) to detect the components of the microreactor effluent. Process efficiency is demonstrated by the achieved yield and the unitary degree of conversion of the limiting reagent. The results reported in the following are the object of a scientific paper published in 2016 in Org. Process Res. Dev.[21]

2.1 Materials and methods

2.1.1 Materials

A mixture of aryl bromide, amine (N-methylpiperazine), and base (potassium tert-amylate) is dissolved in toluene in the presence of an internal standard (4,40-di-tertbutylbiphenyl) and fed in a glass syringe. A solution of catalyst in toluene is loaded in a second syringe, placed on the same syringe pump (Harvard Pump 11 Plus Dual), in order to impose the same flow rate. Both solutions are prepared inside a glove-box under inert atmosphere in the concentrations reported in Table 1. It is worth highlighting that the glove box is refluxed with an inert gas, in particular nitrogen, for about 25 min at 0.9 bar.

The aryl bromide (ArBr) and the palladium-based pre-catalyst are provided by the group of Prof. S.P. Nolan, of the University of St. Andrew UK and are prepared according to the processes reported in literature.[92, 93] The preparation protocol of the aryl bromide is reported in Appendix A. The base (i.e. KOtAm in a solution of toluene in 1.7M (Aldrich)), the amine (i.e. N-methylpiperazine, Met (Aldrich, 99%)), the internal standard (i.e. 4,40-di-tert-butylbiphenyl (Aldrich, 99%)) and toluene (Aldrich,

anhydrous, 99.8%) are commercial products. The concentrations of the reagents is obtained by imposing a quantity of catalyst (mmol) below the solubility limits to prevent the formation of precipitates of the latter which could block the microreactor, as reported in Table I.[20]

Table I *Molecular weights and concentrations in the syringes and in the reactor for the 2-feed configuration.*[19, 20]

Syringe 1	**Mol. weight**	**Quantity [mg]**	**mmol**
Catalyst	1172	23.44	0.02
Toluene	92.14	7.83 (9ml)	0.085
Syringe 2	**Mol. weight**	**Quantity [mg]**	**mmol**
Aryl bromide	344.29	68858	2
N-Methylpiperazine	100.16	220.352	2.2
KO^tAm (solution in toluene 1.7M)	126.24	1110.912	2.1
4,4'-di-tert-butylbiphenyl (I.S.)	266.42	18	0.0675
Toluene	92.14	6.765 (7.765 ml)	0.0733
Tubolar reactor			
Catalyst [%mol] (mol_{cat}/mol_{ArBr})	KO^tAm/ArBr [mol mol^{-1}]	ArBr [M] ($mmol_{ArBr}/ml_{sol}$)	Met/ArBr [mol mol^{-1}]
1	1.05	0.1	1.1

2.1.2 Experimental set-up

A schematic representation of an experimental set-up texted is reported in Figure 2.1. The apparatus has been developed by using the set-up showed by Pommella et al. in 2013[19]. In few words, the mixing is performed in a stainless steel 2 mm i.d. T-junction (i.e. two inlets and one outlet). The reaction takes place in the stainless-steel tubular microreactor with an inner diameter of 2.0 mm and a length of 0.70 m (volume = 2.2 ml), with two syringes to provide the reagents fed in the concentration shown previously in Table I. The microreactor and the junction are heated in a thermostatic bath at a temperature range between 40°C and 80°C, while the feed-syringes are at room

temperature. The reagents are injected into the microreactor by varying the flow rate from 1.1 ml/h to 70 ml/h, in order to have different residence times and, consequently, different conversion degree.

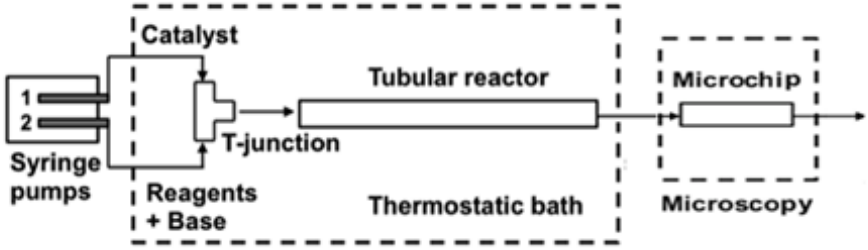

Figure 2.1 *Scheme of the two-feed continuous flow microreactor.*

2.1.3 Analytical method

For analyzing the chemical composition and the real concentration of the effluent, a part of latter (~500μl) for different residence time is picked up in a vial and then analyzed through a Shimadzu GC-FID 2010 GC-MS, equipped with a non-polar capillary column (BPX5 with XO.D. XI.D: 3.05mx1/8inx2.1mm and film thickness from SGE) and He as gas carrier. For the purposes of analysis, the appropriate operating conditions of the GC-MS are set out, Figure 2.2.

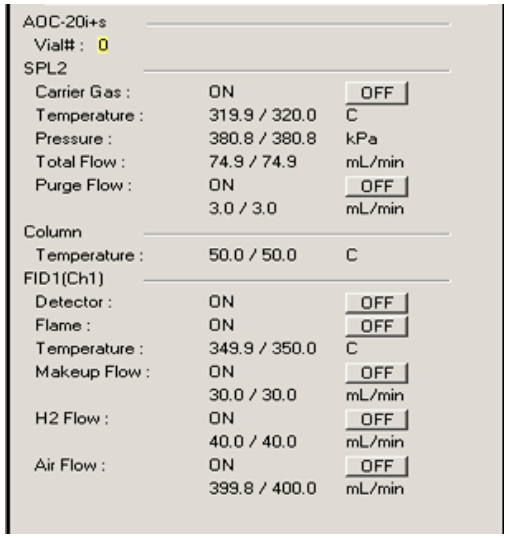

Figure 2.2 *GC-MS operating conditions.*

In Figure 2.2, it can be observed that the analysis is carried out by setting a temperature program so that the temperature column is preserved for 3 minutes at 50°C by using an increasing temperature gradient from 30°C to 360°C and maintained at that temperature for 6 minutes. Following this temperature program, the analysis time is about 30 minutes. It is worth highlighting that to know the retention times of each reagents and to analyse the GC-MS spectrum, different solutions of toluene and reagents (i.e concentrations of 1mg/ml, 10mg/ml and 100mg/ml) are prepared and analysed.

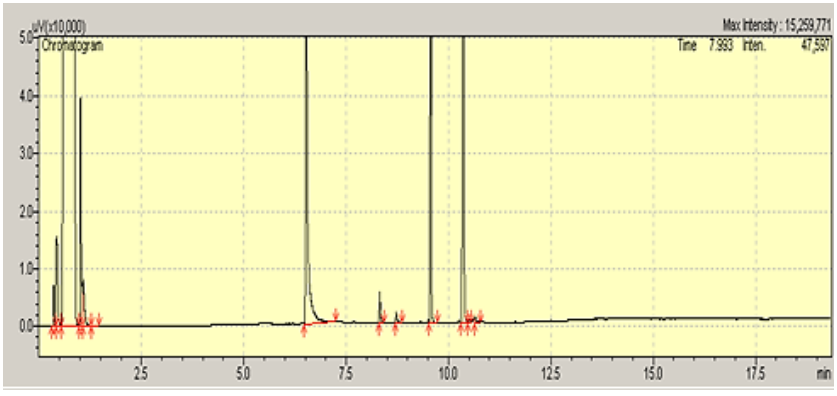

Figure 2.3 GC-MS spectrum. The peaks correspond to the retention (x-axis) of the reagents: N-Methilpiperazine (~1.010min), 4,4'-Di-tert.butylbiphenyl (~8.320min) and aryl bromide (~9.560min).

Finally, by knowing the retention time associated to each reagent it is possible estimated the effluent reagent concentrations by creating a calibration line, reporting on the x-axis the known quantity of the reagent and on the y-axis the area of the peak corresponding to its retention time. By multiplying the angular coefficient of this line for the area of each peak, the mass or volumetric quantity of each substance is obtained. In this way, the conversion degree can be obtained. For this, before the effluent analysis, a first vial containing few drops of feed-syringe 2 (see Table 1) is sent to the GC to determine the initial concentrations of aryl bromide, N-methylpiperazine and the internal standard, and then, in relation to the latter, to obtain the degree of conversion of the limiting reagent (ArBr) according to the residence time within the microreactor.
The ArBr conversion degree is calculated as:

$$Conversion\ degree\ \% = \frac{(mol_{ArBr}^{IN} - mol_{ArBr}^{OUT})}{mol_{ArBr}^{IN}} * 100 \qquad \textit{Equation 19}$$

where $mol_{ArBr}{}^{IN}$ is the amount of ArBr before the reaction and $mol_{ArBr}{}^{OUT}$ is the amount of ArBr after the reaction.

2.2 Results

2.2.1 Effect of catalyst concentration

The first parameter that has been investigated is catalyst concentration, due to the strong impact that the reduction of the amount of catalyst needed could have on process costs and clogging. In fact, the palladium-based catalyst is extremely expensive and, being solid and not completely soluble in toluene, could lead to reactor clogging. The molar percentage of catalyst ranges from 0.16 to 1% (mol/mol), the other components concentration staying unchanged. Data on ArBr conversion degree and on reaction rate are reported in Figure 2.4. As expected, the reaction kinetics decreases by reducing catalysts loading. In fact, for a catalyst concentration of 1 mol%, high ArBr conversion

degrees are obtained (~100%) in about 45 min, while for molar percentage of catalyst of 0.16 and 0.25% (mol/mol) the conversion is not complete, as shown in Figure 2.4a. In addition, in Figure 2.4b, it can be observed a direct linear first-order dependence on catalyst concentration.

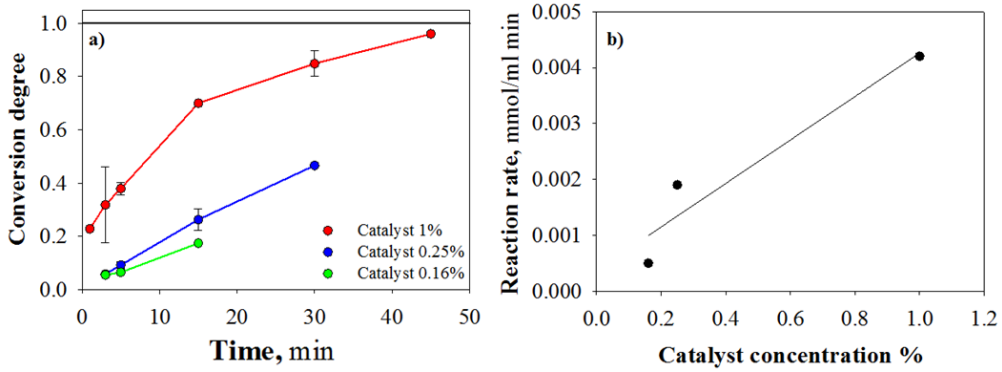

Figure 2.4 *a) Conversion profiles for different catalyst loadings at 50°C. The continuous lines represent full conversion; b) Initial reaction rates for the catalyst concentrations tested.*[21]

2.2.2 Effect of ArBr concentration

The effect of aryl bromide, namely the limiting reagent, has been examined varying its concentration from 0.01 to 0.11M, fixing the other parameters as temperature and catalyst molar concentration (1%). Experimental results on ArBr conversion degree and reaction rate are reported in Figure 2.5. The reaction kinetics increases reducing ArBr loading. In fact, for a ArBr concentration of 0.01M, unitary conversion degree of the aryl bromide is almost immediate, while for high concentrations the completed conversion is obtained in about 45 min, Figure 2.5a. This effect can be explained considering that a lower limited reagent concentration amplifies the effect of catalyst on the reaction (i.e. the active energy E_a of the reaction decreases) and the reaction is promoted. In addition, it is worth noted that the trend of conversion degree for 0.06M and 0.08M is similar. This tendency can be useful to reduce the process costs (i.e. a lower amount of the ArBr). Finally, in the Figure 2.5b it can be observed an inverse linear first-order dependence on the ArBr concentration.

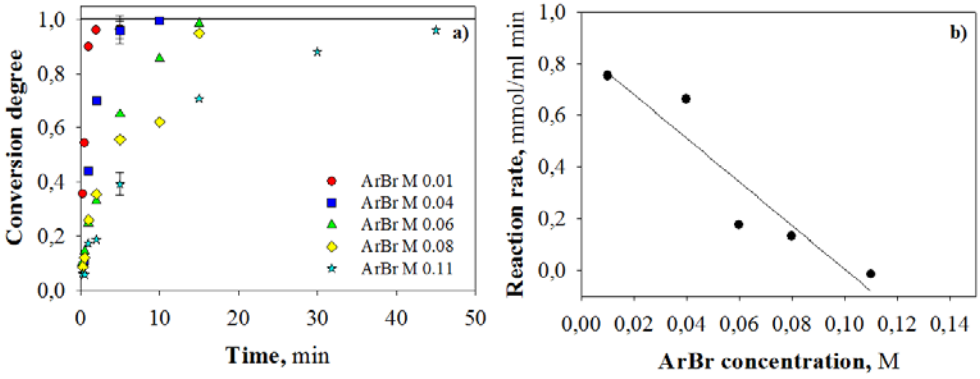

Figure 2.5 *a) Conversion profiles in dependence of the ArBr loading at 50°C. The continuous lines represent full conversion; b) Initial reaction rates for the ArBr concentrations tested.*

2.2.3 Effect of N-Methylpiperazine concentration

The effect of the N-Methylpiperazine is tested varying its concentration from 0.05 to 0.08M, also in this case other parameters being constant. The ArBr conversion degree and the reaction rate reported in Figure 2.6 show that the reaction does not depend on these parameters. In fact, the trend of the conversion degree is equal for each case and the reaction rate is of pseudo-zero order.

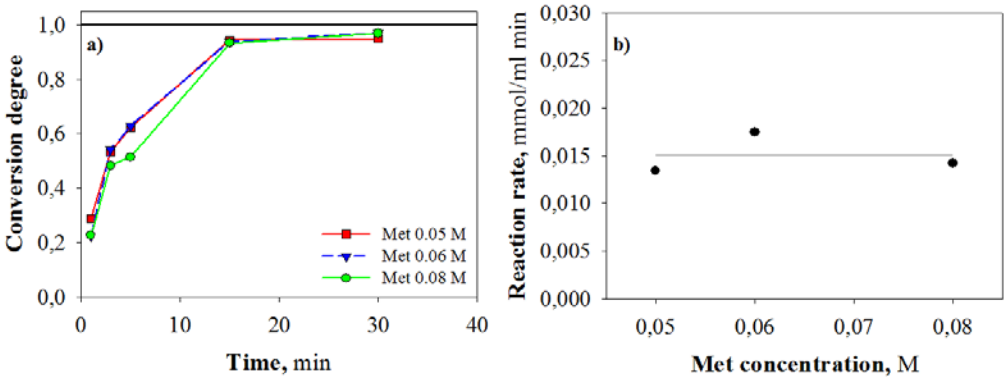

Figure 2.6 *a) Conversion profiles in dependence of the N-Methylpiperazine loading at 50°C. The continuous lines represent full conversion; b) Initial reaction rates for the Met concentrations tested.*[21]

2.2.4 Effect of base concentration

The effect of base concentration on reaction rate is studied modifying only this parameters from 0.03 to 0.116M. From Figure 2.7 it can be observed a direct linear increase of the reaction kinetics because the base encourages the kinetics of the limited step (see the reaction mechanism in Buchwald-Hartwig reaction section).

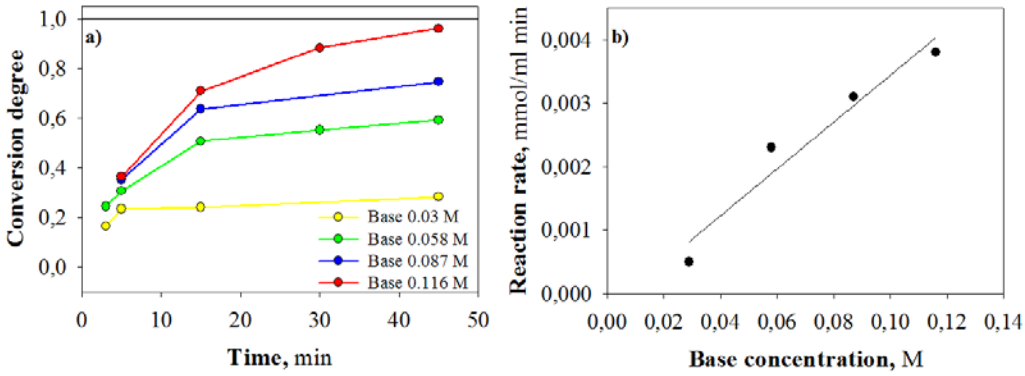

Figure 2.7 *a) Conversion profiles in dependence of the N-Methylpiperazine loading at 50°C. The continuous lines represent full conversion; b) Initial reaction rates for the Met concentrations tested.*[21]

2.2.5 Effect of temperature

Finally, the effect of temperature has been tested. The influence of this parameter on the reaction kinetics is very important. In fact, despite the temperature increment can cause an increase in the kinetics, due to the fact that the reaction is endothermic, an excessive temperature value could lead to high process costs, due to safety issue, and to the degradation of reaction compounds. In Figure 2.8 it can be observed a strong increment of the conversion degree by increasing the temperature. In fact, a soft increase of 10°C from the typical temperature (i.e. 50°C) allows to reach a complete conversion in about 20 min compared with 60min at 50°C.

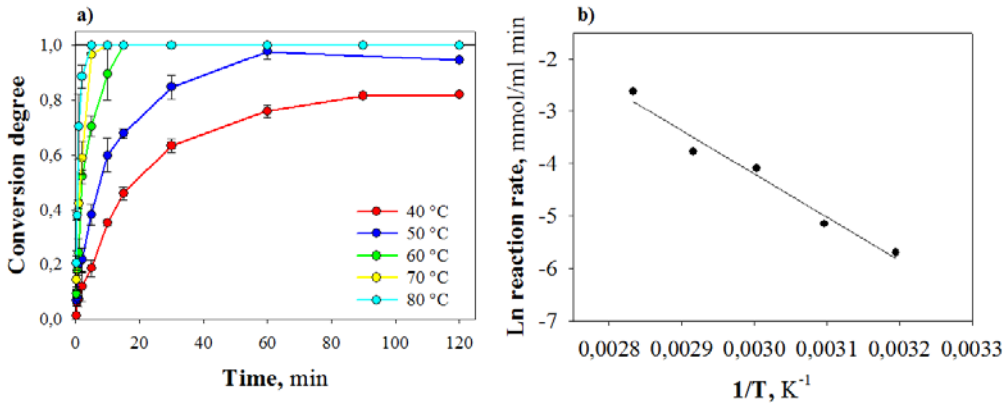

Figure 2.8 *a) Conversion profiles in dependence of the N-Methylpiperazine loading at 50°C. The continuous lines represent full conversion; b) Initial reaction rates for the Met concentrations tested.*[21]

2.3 Conclusion

The intensification of industrial processes through the use of continuous flow reactors has generated considerable interest in the development of novel microstructured systems which can process reactions typically carried out in batch systems. Here, a home-made flow microreactor is presented as innovative device to process and study cross-coupling reactions, with particular attention to Buchwald-Hartwig amination. Exploiting the many advantages of these systems, such as a more efficient heat and mass transport compared to batch systems, the effects of operating parameters influencing B-H reaction kinetic (i.e. catalyst and reagents concentration and temperature) has been reported. In particular, the conversion degree and the reaction rate have been analyzed, resulting in a strong influence of reaction rate on catalyst and ArBr (the limiting reagents) concentration, namely a 1st order kinetics and inverse linear first-order respectively.

Therefore, for the first time, Buchwald−Hartwig reaction has been processed with great success under continuous flow conditions, by using a novel reactor concept which combines the flexibility of batch reactors with all of the advantages of conventional flow systems. The acquired understanding will allow further development of pilot systems able to run also heterogeneous reactions under continuous flow conditions.

3 A microfluidic approach to optimize Buchwald-Hartwig amination reaction

In this chapter, a novel continuous flow microreactor configuration for processing cross-coupling reactions is presented. Major attention is focused on the comparison of the results obtained by the use of the novel 4-feed configuration with the microreactor described in previous chapter. Experiments are carried out by using a stain steel tubular 4-feed microreactor and gas-chromatography coupled to mass spectroscopy (GC-MS). The process efficiency is demonstrated by the achieved yield and the complete conversion of the limiting reagent. Reported results are the object of a paper published in 2015 in RSC Advances.[20]

3.1 Materials and methods

3.1.1 Materials

A solution of catalyst in toluene is fed to a glass syringe, to avoid the corrosion of the syringe walls by toluene. A second mixture of aryl bromide, amine (N-methylpiperazine), and internal standard (4,40-di-tertbutylbiphenyl) is dissolved in toluene and loaded in another syringe. In addition, a third syringe is prepared with the base (i.e. KOtAm) in the toluene. Finally, a fourth feed with only toluene is set to balance the concentration and to make the system more flexible to parameters changes. The four syringes are placed on two syringe pumps (Harvard Pump 11 Plus Dual), imposing the same flow rate on each pump. As described in the previous section, the feed solutions were prepared inside a glove-box under inert atmosphere (i.e N_2) in the concentrations reported in Table 2.

The materials used are the same described in the previous section and also in this case the concentrations of the reagents is obtained by imposing a quantity of catalyst (mmol) below the solubility limits to prevent the formation of precipitates of the latter, which could block the microreactor (as reported in Table II).[20]

Table II *Molecular weights and concentrations in the syringes and in the reactor for the 4-feed configuration.*[20]

Syringe 1	**Mol weight**	**Quantity [mg]**	**Quantity [mmol]**
Catalyst	1172	9.8/21.5/29.3/39.07	0.00836/0.0183/0.025/0.00333
Toluene	92.14	7.83 (9 ml)	0.0849
Syringe 2	**Mol weight**	**Quantity [mg]**	**Quantity [mmol]**
Aryl bromide	344.29	1147.63	3.333
N-Methylpiperazine	100.16	367.25	3.666
4,4'-Di-tert-butylbiphenyl (I.S.)	266.42	18	0.0675
Toluene	92.14	6.74 (7.754 ml)	0.0732
Syringe 3	**Mol weight**	**Quantity [mg]**	**Quantity [mmol]**
KO^{t}Am (Solution in toluene 1.7 M)	126.24	1930	3.645
Toluene	92.14	5.964 (6.85 ml)	0.0647
Syringe 4	**Mol weight**	**Quantity [mg]**	**Quantity [mmol]**
Toluene	92.14	7.83 (9 ml)	0.0849

Tubular reactor				
Catalyst [% mol] (mol_{Cat}/mol_{ArBr})	**Catalyst** [M] $*10^{-4}$ ($mmol_{Cat}/ml_{Sol}$)	**ArBr** [M] ($mmol_{ArBr}/ml_{Sol}$)	**Met/ArBr** [mol/mol]	**KO^{t}Am/ArBr** [mol/mol]
0.25/0.55/0.75/1	2.4/5.3/7.2/9.6	0.1	1.1	1.09

3.1.2 Experimental set-up

A schematic representation of the 4-feed reactor is reported in Figure 2.1. The apparatus has been developed by re-modelling the set-up showed in the previous paragraph[21]. In this case, therefore, the mixing is performed in a stainless steel 2 mm i.d. junction, with four inlets and one outlet. The reaction takes place in a stainless-steel tubular microreactor with an inner diameter of 2.0mm and length of 0.70m (volume = 2.2ml), with four syringes, to provide the reagents fed in the concentration shown previously in Table II. The microreactor and the junction are heated in a thermostatic bath at 50°C, while the four syringes containing reagents, catalyst, base and solvent are at room

temperature. In addition, the reactor effluent is analyzed by Shimadzu GC-FID 2010 GC-MS with the protocol previously described in Analytical method paragraph.

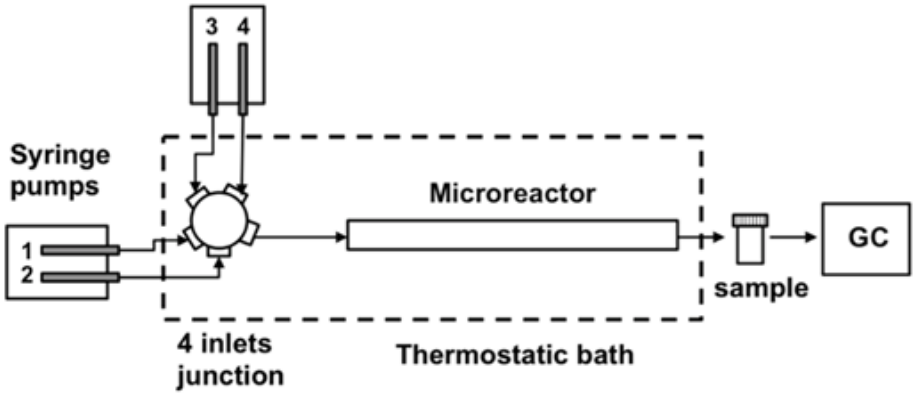

Figure 3.1 *Scheme of the four-feed continuous flow microreactor.*

3.2 Results

3.2.1 Continuous flow reactor configurations

In this section, the work is focused on the development of a new optimal configuration for the reactor system previously presented (Figure 2.1), with the purpose of make the microsystem more flexible in terms of changes of the operating conditions, such as reagents concentration. To do this, various configurations have been developed, to separate the base from the remaining components of the system (to dilute mainly the base, which presents precipitation problem due to oxidation) and to add a separate flow consisting solely of the solvent, Figure 3.2.[20]

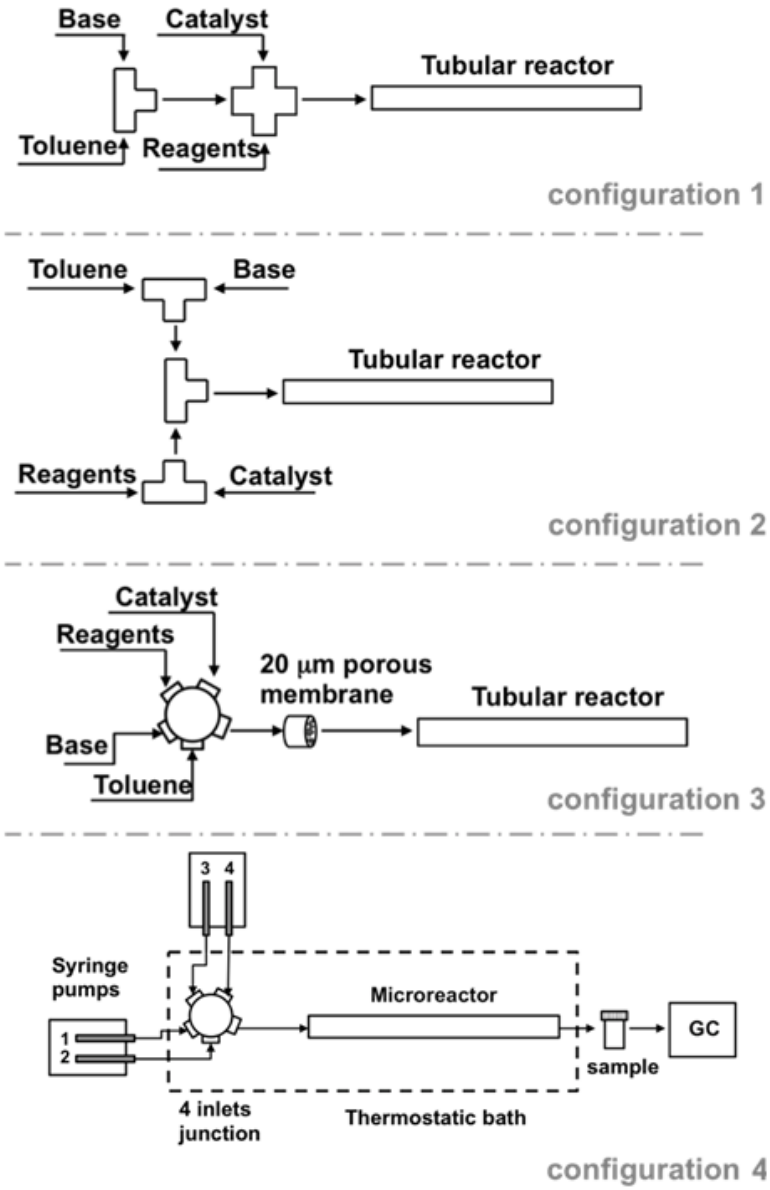

Figure 3.2 *Schematics of different configuration used to increase the flexibility of the flow reactor.*[20]

In Figure 3.2 it can be observed that the four syringes are set on two syringe pumps and are connected to the microreactor by using different design: ***configuration 1*** in which preliminarily the toluene and the base are mixed by a T-junction and then connected to the other two syringes by a cross junctions (*configuration in series*); ***configuration 2***

where the feeds are connected in pairs to microreactor between three T-junctions (in this way the catalyst and the base are more dilute before the entry into the reactor (*configuration in parallel*); ***configuration 3,*** in which the 4 solutions are attached by a junction with four inputs and one output to a porous membrane (with pores of 20 μm) and then connected to the microreactor; ***configuration 4,*** where the 4 mixtures are directly linked with the reactor by the junction described in configuration 3.

The experiments showed that the first three configurations present clogging problems at short residence time, which are not found in the two-feed system previously proposed. This is likey due to the low dissolution of the catalyst (initially solid) due to the weak mixing and/or the large amount of KBr produced. In addition, in order to verify the best configuration, when the reactor is not clogged, the degree of conversion of the limiting reagent (ArBr) is analysed and compared to the set-up texted in the previous section, Figure 3.3.

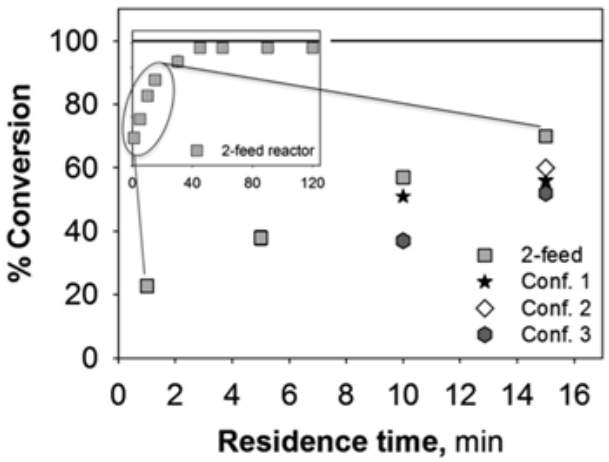

Configuration 1			Configuration 2			Configuration 3		
Time [min]	Flow rate [ml/hr]	% Conversion	Time [min]	Flow rate [ml/hr]	% Conversion	Time [min]	Flow rate [ml/hr]	% Conversion
7.5	4.4	Blocking	7.5	4,4	Blocking	7.5	4.4	Blocking
10	3.3	51 ↓	10	3.3	Blocking	10	3.3	37 ↓↓
15	2.2	56 ↓	15	2.2	60 ↓	15	2.2	52 ↓↓

Figure 3.3 *Conversion degree as a function of time for the three-feed configurations showed in Figure 3.2 in comparison with the two-feed system at short residence time. The overall conversion of the reaction run in the two-feed reactor is reported in the inset. In the table, black arrows indicate that the conversion degree is lower (one arrow) and much lower (two arrows) compared with the two-feed reactor system.*[20]

Comparing the conversion degrees reached by varying the residence time, it can be observed that the performances of the first three configurations are lower than the ones of the two-feed system. For this reason, to improve the mixing and the performance of the reactor configuration 4 has been designed (Figure 3.2 *configuration 4*). This system does not present clogging, leading to conversion degrees close to those of two-feed configurations at different residence time, as shown in Figure 3.4.

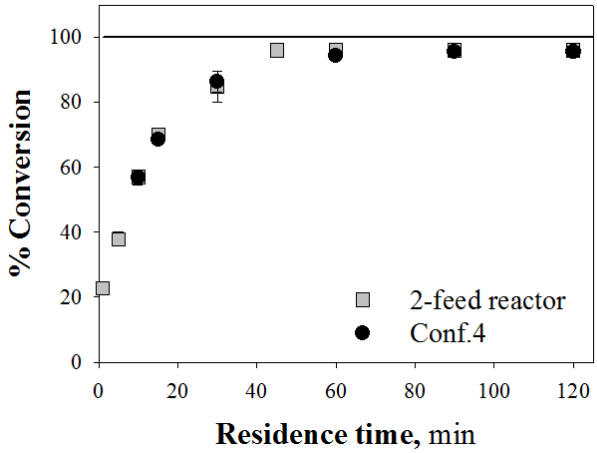

Figure 3.4 *Comparison between 2-feed and 4-feed (configuration 4) reactor operating at 50°C with 0.1 mol% of the catalyst.*

3.2.2 Effect of catalyst concentration

The molar percentage of catalyst which is investigated ranges from 0.16 to 1% (mol/mol), while the other parameters are fixed. Corresponding results on % ArBr conversion degree are reported in Figure 3.5. As expected, the reaction kinetics decreases by reducing the catalysts loading. In fact, at the highest catalyst loadings (1-0.5 mol%), the reaction is almost complete (98%) after 60 min and 120 min respectively, while for lower catalyst concentration (0.25 mol%), complete conversion is never reached. Is worth highlighting that decreasing the catalyst concentration and reaching high product yield at the same time lead to the reduction of the overall costs of the process. In this case, it can be observed that a 0.75% molar concentration of the catalyst allows to obtain performance similar to 1.0% molar at the same residence time.

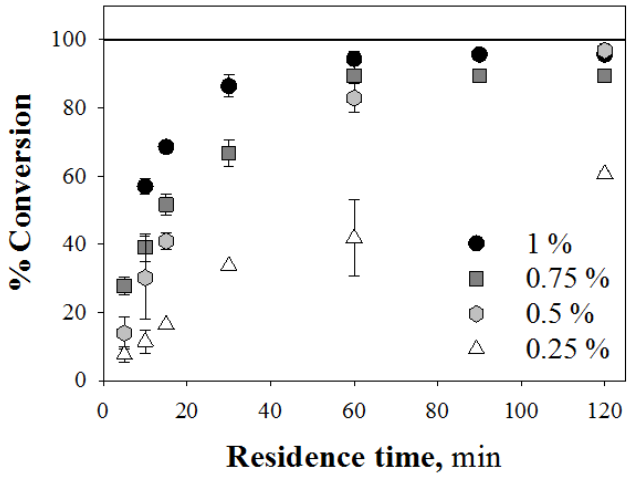

Figure 3.5 *Conversion profiles for different catalyst loading at 50 °C with a concentration in the reactor of 0.1M of Aryl bromide (toluene 32.6 mL). The continuous lines represents the full conversion.*[20]

3.2.3 Effect of ArBr concentration

The effect of aryl bromide is examined varying its concentration from 0.01 to 0.11M, while the other parameters stay unchanged. By plotting ArBr conversion degree vs residence time (Figure 3.6) it can be observed that the reaction kinetics increases by reducing ArBr loading. In fact, for an ArBr concentration of 0.01M, the complete conversion of the aryl bromide is almost immediate, while at the highest concentration complete conversion is obtained in about 80 min, Figure 2.5a. This could explain why a faster reaction rate at lower ArBr concentrations is found.

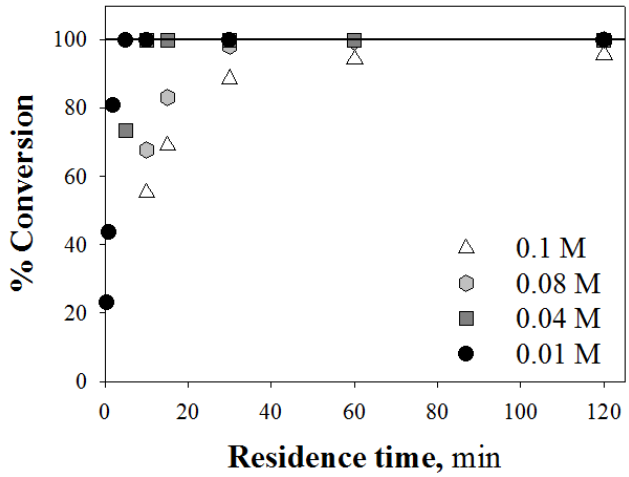

Figure 3.6 *Conversion for different Aryl bromide concentration at 50 °C with a concentration in the reactor of 9.6*10-4 M of catalyst. The continuous lines represents the complete conversion.*[20]

3.2.1 Effect of temperature

Ultimately, the effect of temperature is tested by varying it from 50°C to 70°C. For the latter, a full conversion is achieved in 10 minutes, whereas 1 hour is needed at 50 °C (Figure 3.7). This effect is due to the higher solubility of the solid compounds which improves the solution mixing. Increasing the temperature in the microreactor and, therefore, by enhancing the reaction kinetics it is possible to reduce the catalyst concentration, this representing enormous advantages in terms of costs.

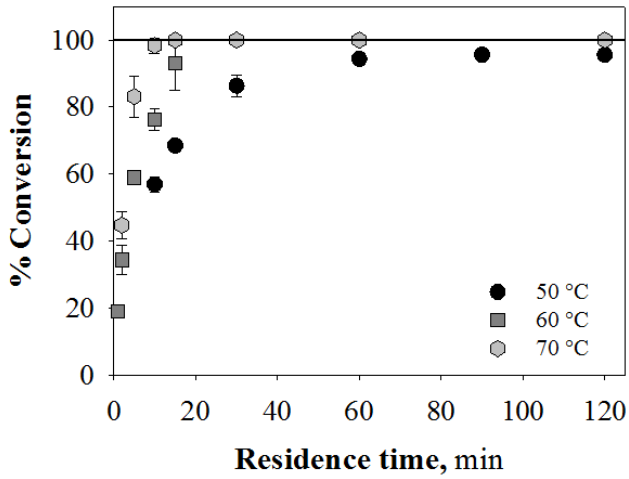

Figure 3.7 *Conversion profiles for different temperature concentration in the reactor for 1% of catalyst. The continuous lines represent the complete conversion.*[20]

3.3 Conclusions

The increasing attention on the continuous flow operations in fine chemical and pharmaceutical synthesis, thanks to the advantages over traditional batch processing in terms of efficiency, safety, product quality and sustainability has implicated the development of the novel microfluidic designs in flow chemistry.

Therefore, the aim of this work is to develop and to realize a home-made continuous flow microreactor by optimizing a microfluidic configuration widely analyzed in the previous task to process Buchwald-Hartwig cross-coupling reaction. Various configurations are proposed for the purpose of achieving the optimum design and flexibly to changes of operating conditions. In addition, the conversion degree of the limiting reagent is compared to the one of the two-feed configuration, showing that there is any substantial difference between the two-experimental apparatus in terms of conversion of the limiting reagent and selectivity. However, using this novel system, there are several benefits, including greater flexibility in the variation of reagent concentration, the ability to separate the base from other compounds and the addition of

a stream containing only the solvent, thus making the system more inclined to possible variations in process conditions.

In conclusion, this study provides the methodology to optimize cross-coupling reaction by using a home-made continuous flow microreactor. The choice of such a microfluidic approach meets requirements of green chemistry, in terms of productivity, process handling, economics savings and operations safety.

4 The effect of shear flow on microreactor clogging

In this chapter, a direct visualization of particles adhesion to the wall, cluster growth and reactor clogging in a microfluidic system is approached, exploiting the knowledge acquired by the work described previously. The effect of shear flow on cluster growth kinetic and on the morphology of KBr aggregates is investigated at different flow regimes. Images of the resulting morphologies are then presented and compared.

4.1 Materials and methods

4.1.1 Experimental set-up

A schematic representation of the experimental set-up is reported in Figure 4.1. The materials for the reaction and the experimental apparatus has been developed using the set-up showed previously in the Figure 2.1 of the chapter 2.0 (pg. 29). The reaction takes place in the stainless-steel tubular microreactor with an internal diameter of 2 mm and two feed-syringes to provide the reagents fed in the concentration shown previously. In order to allow the visualization of cluster formation and morphology, the reactor has been connected to a glass microchip through a PEEK tubing of 1mm i.d. and a fused silica tubing of 350μm i.d. The microchip, a commercial glass chip (Micronit) containing rectangular cross section channel (500x100μm), is placed under a transmitted-light microscopy (Axio 100, Zeiss) equipped with a high-speed video camera (Phantom 4.3, capable to record up to 10000 frames/s) with a 10x objective, Figure 4.1.

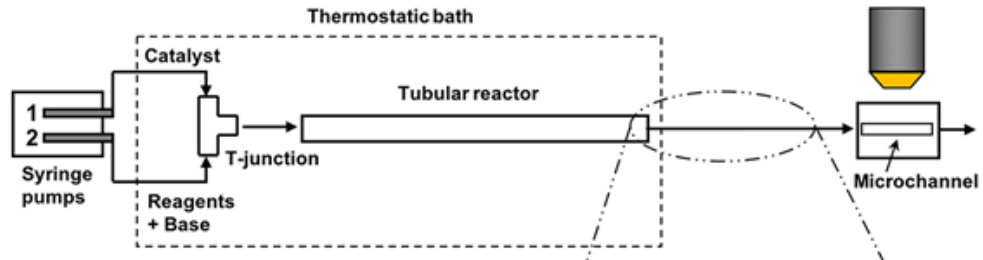

Table II: Specific of microfluidic system elements.

Experimental component	D [mm]	Length [mm]	Material
Tubular reactor	2	700	Stainless steel
Tubing A	1	200	PEEK
Tubing B	0,35	50	Glass
Microchannel	0,5x0,1*	7	Glass

* refer to rectangular channel width and depth respectively

Figure 4.1 *Scheme of the experimental apparatus.*

The apparatus is installed on an anti-vibration table. Images are then processed by a commercial software, Image Pro-Plus® 6.0 (Media Cybernetics, Silver Spring) with a home-made macro (see Appendix B), in order to measure the cluster area, the cluster intensity (optical density OD) of each image at different times. Moreover, images in stationary condition are acquired by using an inverted Confocal Laser Scanning Microscopy (Zeiss, CLSM Pascal) using a 10x objective (Zeiss Plan-Neofluar, image size 898.24x898.24μm) connected to a motorized focus system controlled by a dedicated software (Pascal), and two laser excitations (He-Ne at a wavelength of 543nm, or Ar at 488nm).

4.2 Results

4.2.1 Particle aggregation and cluster growth

First of all, the attention is focused on the study of the effect of flow rate on particle aggregation. For this, two preliminary analyses are carried out: i) SEM imaging and elemental analysis of the aggregates present onto microreactor inner surface and ii) optical microscopy analysis of cluster coming out from the reactor and from the tubing connecting the reactor and the microchip. For the first case, Scanning Electron Microscope (SEM) observations show a granular structure of the aggregates (Figure 4.2)

that cover completely the inner surface of the reactor, which has a high roughness that favours the deposition of solid particles. Furthermore, the Energy Dispersive X-ray (EDX) analysis has revealed that the aggregates are consisted mainly of K and Br, the by-product produced by B-H reaction.

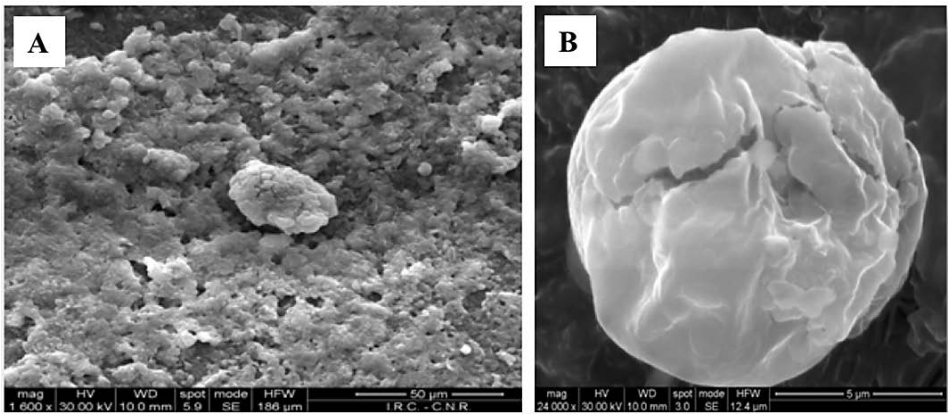

Figure 4.2 *SEM images of the fouling layer covering the inner surface of the stainless-steel tubular microreactor (A) and of a spherical KBr particle (B). Scale bar: A. 50μm and B. 5μm.*

In order to investigate cluster morphology coming out from the reactor and the connection tube, several samples are collected and analysed in brightfield (BF) mode for different flow rate. In Figure 4.3 can be seen that there is any substantial difference between the aggregates outgoing from the reactor and the connection tube, therefore the transition from a section of 2 mm i.d. to one of 1mm i.d. does not affect the structure of the cluster.

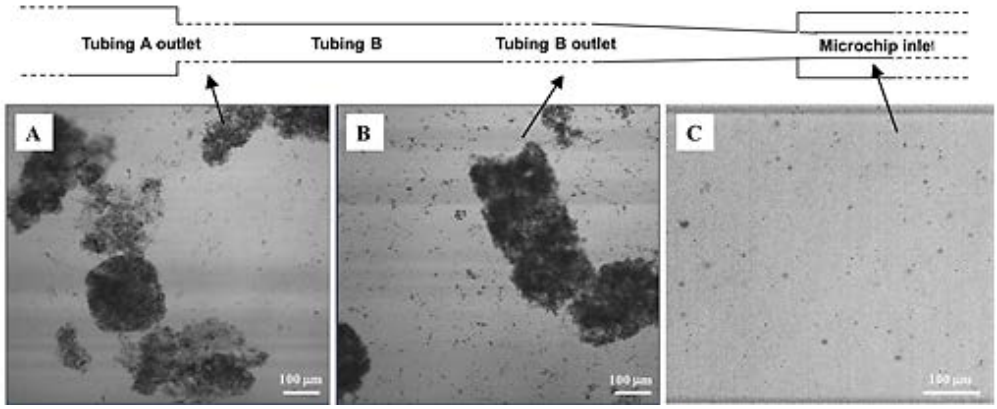

Figure 4.3 *Top: Schematic of the tubing connecting the microreactor to the glass microchip. Bottom: Bright-field images of cluster at the outlet of tubing A and B and inside the glass microchip at the inlet of the channel (image C).*

However, the variation of section between the cylindrical shape of the connecting tube of 1mm i.d. and the rectangular channel of 170μm i.d. of microchip likely leads to the complete breakage of the aggregates (Figure 4.3c). The lack of aggregates at the chip inlet is probably due to their disruption under strong elongational flow in the converging zone present between the tube and the microchannel.[94]

At this point, the evolution of the fouling process inside the glass microchip as a function of Reynolds number (Re) and time has been studied for two Re numbers (i.e. Re=1.5 and Re=15), which ensure laminar flow conditions and a uniform distribution of particles along channel width and depth, Figure 4.4. In Figure 4.4 it can be observed the first two phases of fouling described in the paragraph 1.2 *Fouling and clogging*, namely particle adhesion to channel wall and cluster growth. For the acquisition of the images time 0 is considered as the time at which the first salt particle adhered to the wall channel. It is possible to observe that cluster formation starts at the wall and that the higher the Re, the faster particle adhesion to the wall occurs. Considering the frame at 30s in Figure 4.4, only few particle/wall adhesion sites are present at Re=1.5, while at Re=15 the number of adhesion sites increases considerably. This somehow counterintuitive result could be explained by a fast and strong particle adhesion to the wall: once a particle gets into contact with the wall, it adheres to this location and creates a nucleation site for further attachment of other particles. According to this explanation, higher values of Re

promote faster wall adhesion because of the higher contact frequency associated to a higher flow rate. Surprisingly, cluster growth follows an opposite trend: indeed, at small Re, although the number of adhesion sites is smaller, cluster growth is faster and formation of larger aggregates occurs in shorter time (see for example the frame at 30s in Figure 4.4). This would imply that particle-particle attractive forces in an aggregate are weaker than particle adhesion to the wall.

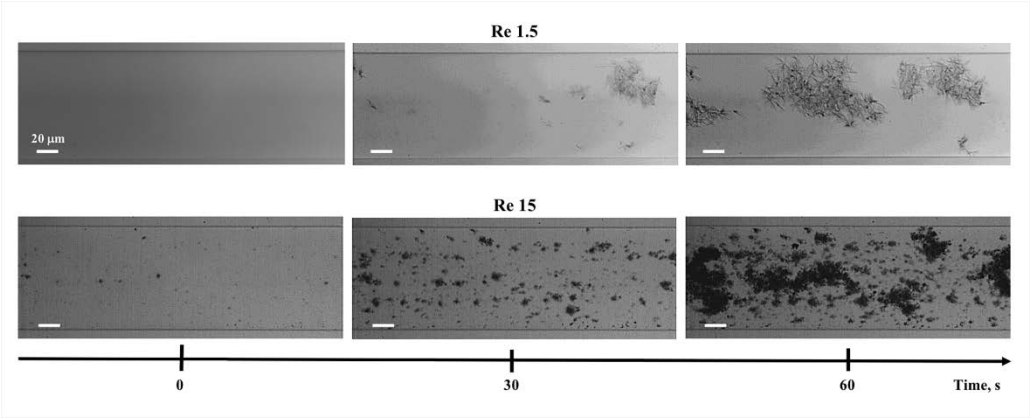

Figure 4.4 *Images representing cluster formation and growth at Re 1.5 (top) and Re 15 (bottom) as a function of time.*

Growth kinetics of individual clusters is analysed in a quantitative manner by using a macro written in the programming environment of a commercial software for image analysis (see Appendix B). The analysis of a given cluster has been carried out by using a two-step fully automated procedure. The first step is used to: (i) select the frame containing the initial site of adhesion and aggregation by applying a grey level threshold, i.e., by comparing the average grey level of each image to the background value. It should be pointed out that, due to low particle concentration, the first frames are empty and only few sites per time are found in the field of view. (ii) extract and record cluster parameters (i.e. area and density). In this manner, it is possible to analyse all clusters contained in an AOI (area of interest) in just a few minutes. An example of image processing is reported in Figure 4.5 (left), where it is evident that cluster growth rate at Re=1.5 is considerably faster than that at Re=15. It is important to underline that clusters

are selected at the same position along the channel width, to avoid any effect related to the flow profile.

A quantitative analysis of cluster growth as a function of Re and time is presented in Figure 4.5 (right), where cluster area is plotted as a function of time. The error bars are the standard deviation over 5 clusters per measurement and for cluster at the same position along the channel width. While the cluster area at both Re=1.5 and Re=15 increases with time, the values at Re=1.5 are higher than the ones at Re=15 across the entire range of time. For this analysis, time 0 corresponds to the time at which the particle under examination adheres to the channel wall.

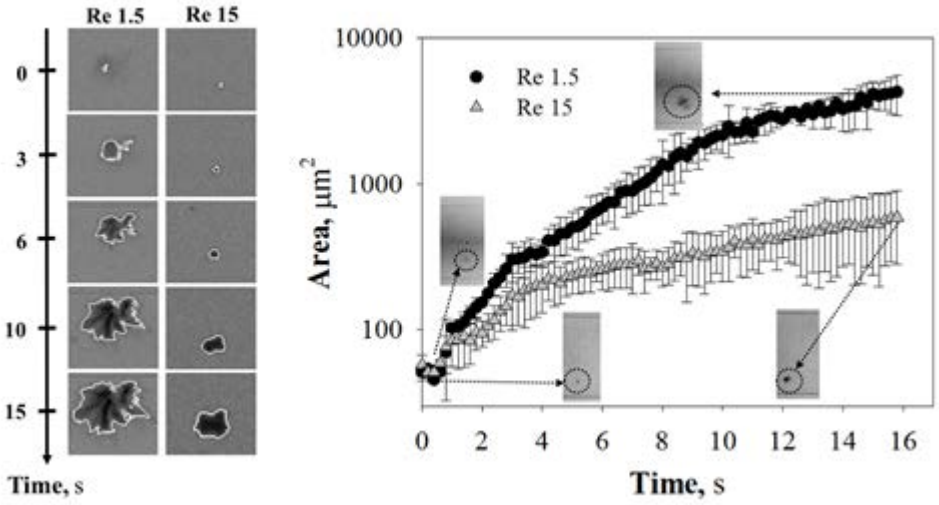

Figure 4.5 *Single cluster growth kinetic as a function of time and Re.*

The formation of an apparently stable cluster (i.e. with a steady-state size at a given shear rate) results from a balance between particle aggregation and cluster break-up or erosion. Aggregation rate is dependent on the frequency of particle collisions (which depends on the flow field) and on the height of the energy barrier which, in turn, is determined by the nature of particle interactions. Similarly, cluster breakage is affected by the force exerted by the incoming fluid (and so by the flow field) and by the strength of particle-particle interactions.

As shown in Figure 4.6, which shows BF images of the cluster attached on the channel walls and SEM images of samples collected at the exit of the glass channel and dried, the flow field also affects cluster morphology and compactness. In particular, aggregates at Re=1.5 are made of needle-shaped crystals, forming a sort of “dendritic” low density, star-like structures, whereas clusters formed at Re=15 appear as compact structures likely made of spherical particles.

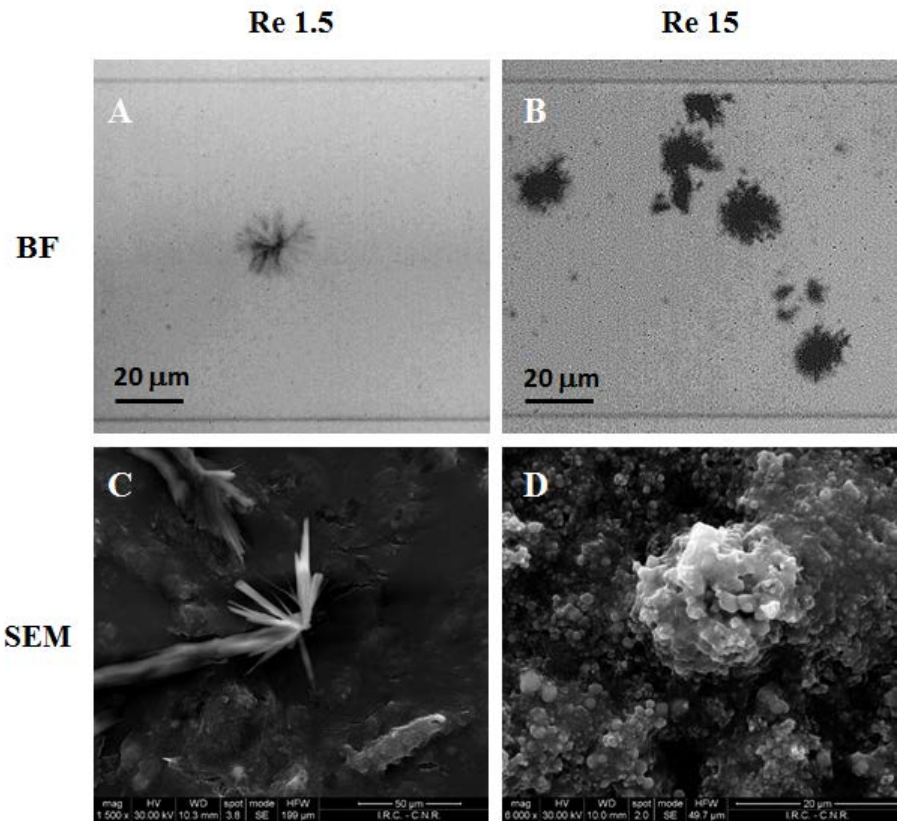

Figure 4.6 *Cluster morphology as a function of flow strength. Top) optical image of the deposited crystals having dendritic-needle like shape for Re=1.5 A) and dendritic-like irregular shape within the glass microchannel for Re=15 B); bottom) scanning electron microscopy (SEM) image of the deposited crystals having dendritic-needle like shape for Re=1.5 C) and dendritic-like irregular shape within the glass microchannel for Re=15 D).*

This effect can be explained taking into account two factors, the particle diffusion in the channel and the chemical interaction between the particle and channel walls. The first

can be investigated with the Pe number (see 1.1 Microreactors paragraph). In fact, when Pe is low (i.e. Re=1.5 or namely Pe~10^2) diffusion predominates on advection, the deposits are made of dendritic-needle like crystals (Figure 4.6 Top A and Bottom C), ordinated structures because the particle have all the time to arrange among them and to form clusters with neat and symmetrical structures. Otherwise, when Pe is increased of an order of magnitude (Re=15 and Pe~10^3), and hence the main fluid velocity in increased, the crystalline order of the structure is largely lost and, even though they still seem to have a dendritic shape, from a more macroscopical perspective (optical imaging, (Figure 4.6 Top B), they actually appear to be disordered and highly packed when having a closer look (SEM imaging, (Figure 4.6 Bottom D) to their structure, because the advection predominates and the cluster structure is given only by the collisions of the dragged particles.

The chemical interaction between the particle and channel walls, therefore, can be studied taking into account the chemical composition of the aggregates effluent by EDX analysis. In this way, the presence of potassium (K) and oxygen (O) for cluster at Re=1.5 and of K and bromide (Br) at Re=15 has been respectively highlighted. This different chemical composition of clusters can be explained considering the thermodynamic equilibrium between the by-product KBr and the base KOtAm, Figure 4.7, where the KOtAm formation is favored over the potassium bromide. Considering the latter for low Re (i.e. Re=1.5) the mixture shows a strong concentration of the base and low concentration of KBr, while for high Re (i.e. Re=15) the contrary can be observed.

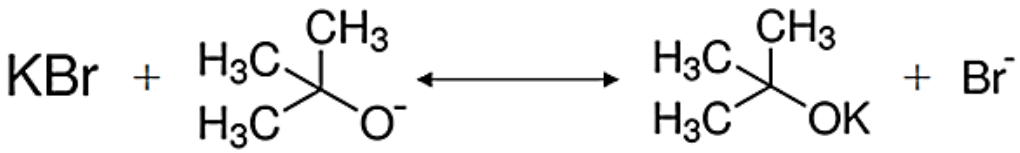

Figure 4.7 *Thermodynamic equilibrium between KBr and KOtAm.*

In addition, that the potassium ions tend to interact with the hydroxyl groups of the channel glass walls, making the cluster structure dependent on the chemical species

connected at it. In fact, under flow KOtAm tends to form needle-like structures while KBr has a disordered arrangement. To further confirm the hypothesis suggested by XRD analysis, i.e that the dendritic-needle like deposited structure are related to KOtAm, a suspension containing the same compounds of the chemical reaction apart from the arylbromide, is flowed in the glass microchannel, thus preventing the formation of KBr. The results are reported in Figure 4.8 and show again dendritic needles, thus confirming the hypothesis that such crystalline structures are made of KOtAm. The crystallinity of such structures is emphasized by their birefringence as obtained by polarized optical microscopy (POM).

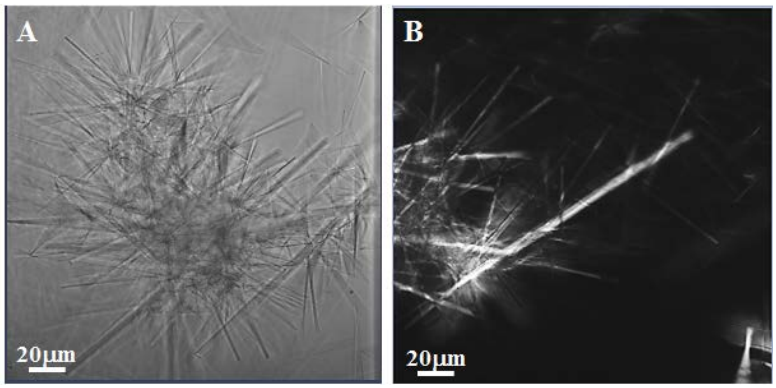

Figure 4.8 *Dendritic-needle like structures deposited within the glass microchannel in the absence of KBr and ArBr. A) Optical microscopy image with 40x magnification and Bf) POM images magnification, evidence of crystals birefringence. Each are acquired with 40x magnification.*

In Figure 4.9 a quantitative analysis of the optical density as a function of time is presented. Optical density (OD) is defined as the ratio of transmitted to incoming light and it can be expressed by the following equation:

$$OD = \frac{\overline{I_B} - \overline{I_C}(t)}{\Delta I}$$

where $\overline{I_B} - \overline{I_C}(t)$ is the difference of the mean intensity (expressed by the mean gray level) of the image background $\overline{I_B}$ and that of the cluster $\overline{I_C}(t)$ at each time. This quantity

is made dimensionless by the difference ΔI= $\overline{I_B - I_C(t)}$ which represents the average value of the difference $I_B - I_C(t)$. OD can be taken as representative of cluster compactness or density. The opaquer is an object, the higher is its optical density and the darker it appears in bright-field microscopy. Therefore, optical density can be seen as an indirect measure of structure compactness. Optical density as a function of time shows an increasing trend both for Re=1.5 and Re=15. Moreover, the data at Re=15 are higher than the ones at Re=1.5 in the entire time range investigated and show a steeper slope, suggesting that low Re leads to the formation of less dense and compact structures. This is likely due to the fact that flowing particles have enough time to build an ordered configuration and erosion effects are less effective, contrary to what happens at higher Re where a dynamic balance between aggregation and breakup leads to more compact and spherical structures.

The product of cluster optical density and cluster area provides some information about the mass of the aggregates. At Re=1.5, clusters are larger (Figure 4.5) and less dense (Figure 4.9A) than clusters at Re=15. In Figure 4.9B the product of optical density and cluster area is plotted as a function time: data at Re=1.5 almost superimpose to the ones at Re=15, indicating that the clusters have more or less the same mass, irrespective of the imposed flow field.

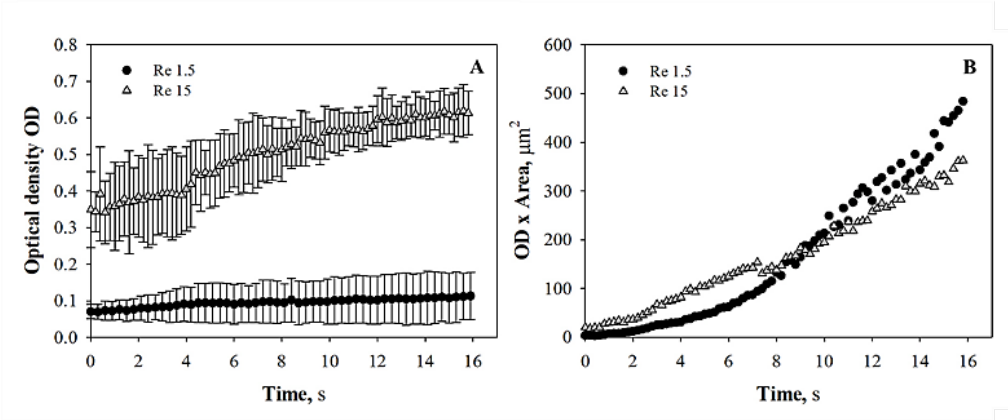

Figure 4.9 *Optical density (A) and Optical density x Area (B) as a function of time at Re 1.5 and Re 15.*

Finally, another quantitative analysis based on fractal theory (see Fractal theory section 1.2.4 pg. 19) is conducted, in order to determine the fractal dimension as an index of compactness of the cluster and the number of particle per cluster. In fact, by knowing cluster perimeter and it is possible to evaluate the primary particle dimension (d_{pf}) which is directly correlate to the fractal dimension, d_f (see Equation 13b and 14b), Figure 4.10.

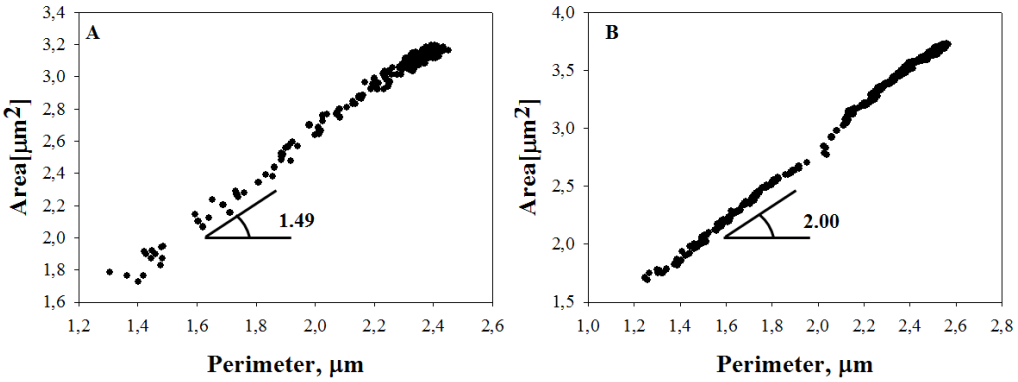

Figure 4.10 *Cluster area as a function of the cluster perimeter for Re=1.5 A) and Re=15 B).*

In Figure 4.10, d_{pf} can be taken as the slope of area vs perimeter plot, resulting in 1.49 for Re=1.5 and 2.00 for Re=15. Using the so obtained values of d_{pf} in Equ. 14b, it is possible to evaluate d_f as equal to 2.00 and 2.7 respectively. These value, therefore, show that for each Re numbers the agglomerate can be considered as a fractal (i.e. the values respect the fractal range from 1 to 3) and the agglomerates for high Re numbers present a more compact structure compared to low Re numbers, that is for Re=15 d_f is about 3.00. In addition, using Equation 15 the number of primary particle into the cluster (N_p) has been evaluated. In Figure 4.11 it can be observed that for high Re numbers N_p is higher compared to the one of low Re numbers, because, as seen previous, after a preliminary trend for Re=15 the particle-cluster collisions are higher compared to Re=1.5 and the cluster area increases quickly. Furthermore, the N_p curve for Re=1.5 highlights probably an equilibrium between aggregation and breakage forces for high time (i.e a constant value).

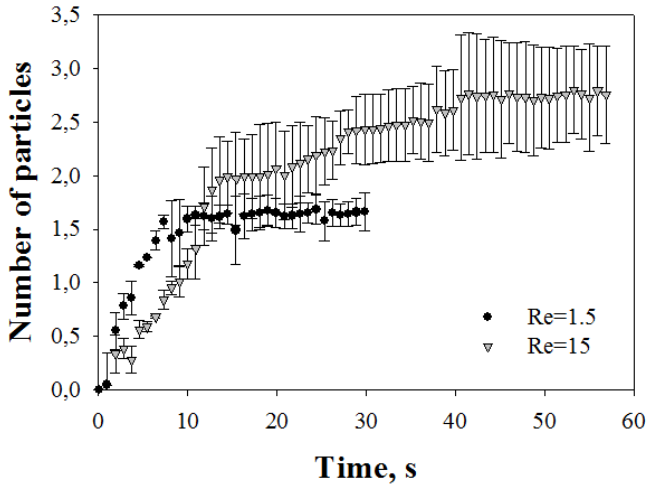

Figure 4.11 *Number of primary particles (N_p) into the cluster as a function of the time.*

4.2.2 Microchannel clogging

Taking into account that as time moves forward the clusters area increases and the free space viable by incoming particles is reduced, i.e. the number of particle-cluster collisions increases and the effective section of the channel reduces, the attention is focused on the study of clogging channel. In fact, a qualitative analysis of the images of the clogged channel by BF and POM mode confirms that, even at long times, the structures formed at Re=1.5 are less dense (and so more transparent to light) as compared to the ones formed at Re=15, thus showing again how the imposed flow field strongly affects formation and stability of micro-particle aggregates, as shown in Figure 4.12.

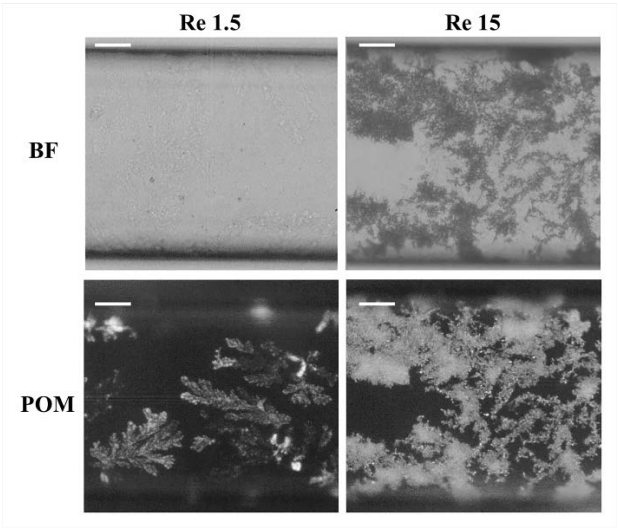

Figure 4.12 *Optical microscopy (up) and POM (down) images of clogged channel. Scale bar: 100 μm.*

Since the density of the aggregates increases with Re, the time needed to clog the channel is dependent on Re as well. This is shown in Figure 4.13 by plotting the percentage of clogging (i.e. the area occupied by clusters with respect to the total area of the channel) as a function of time. After an initial growth, which is similar for the two Re, the data at Re=15 follow a steeper trend as compared to the data at Re=1.5 (the slope at Re=15 is 0.6 while the slope at Re=1.5 is 0.06). Moreover, data at Re=15 eventually approach a plateau value, indicating that no more growth is possible due to channel clogging (as shown in the inset of Figure 4.13). On the other end, the time required to reach the clogging of the channel at Re=1.5 is much longer (i.e. about 15 min), which can be related to the less compact structures formed in these flow conditions. So, a clogging of 65% is reached after 15 min at Re=1.5, while it takes only 3 min at Re=15.

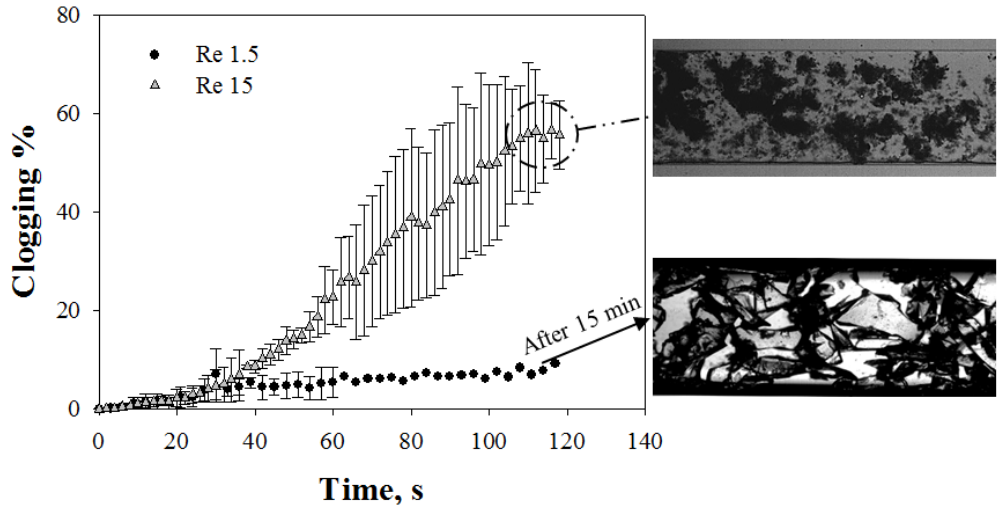

Figure 4.13 *Percentage of channel clogging as a function of time at Re 1.5 and Re 15. Scale bar 100 μm.*

The 3D reconstruction of clogged channel in Figure 4.14 has been obtained by z-stacks of images acquired by confocal laser scanning microscopy (CLSM). The bright structures are the KBr clusters and x-y is the horizontal plane. The channel depth (i.e. along z direction) appears mostly occupied by the clusters. Moreover, these images confirm the formation of less dense structures at Re=1.5 and denser at Re=15.

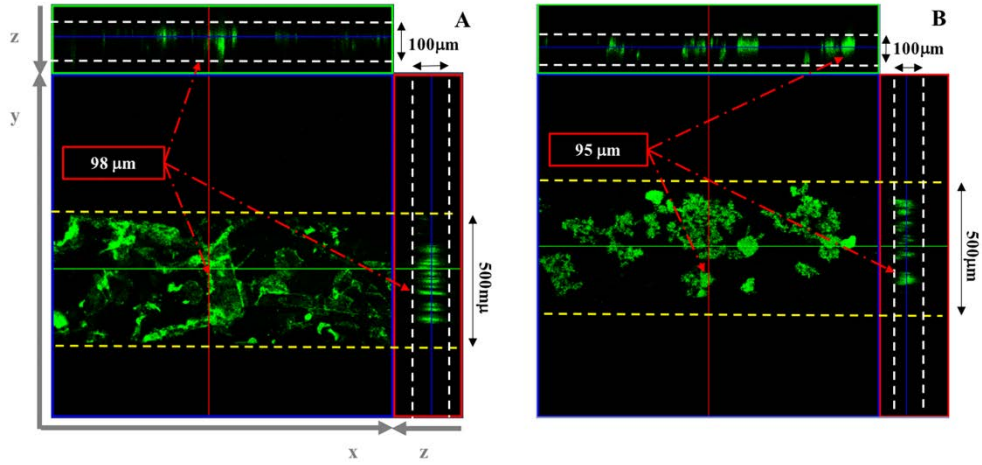

Figure 4.14 *Confocal microscope (LSM Pascal 510, Zeiss) images of clusters formed at Re 1.5 (A) and Re 15 (B).*

4.3 Conclusions

Literature is strongly focused on the characterization and the knowledge of cluster aggregation and in particular on the clogging of microstructured devices. In this work, mechanisms leading to channel wall fouling and cluster growth are investigated by optical and electron microscopy. An innovative microfluidic-microscopy set-up is also developed. Aggregation kinetics of suspended cluster from the Buchwald-Hartwig reaction in microchip at different flow rate have highlighted the important role of the latter on fouling rate and on cluster morphology. Two Re numbers are considered (i.e. Re=1.5 and Re=15), both ensuring laminar flow regime and a uniform distribution of particles along channel width and depth. At each Re particle adhesion to channel wall and cluster growth can be observed. It has been shown that cluster formation starts at the wall, likely due to the velocity profile, which promotes particle/wall interactions. The higher is Re, the faster is particle adhesion to the wall due to the increased frequency of particle/wall collisions and particle adhesion to the channel surface. Once a particle has adhered to the wall, it sticks there, allowing the attachment of other flowing particles. Surprisingly, cluster growth follows an opposite trend: indeed, at small Re, although the number of adhesion sites is smaller, cluster growth is faster, leading to the formation of larger aggregates in less time. Moreover, the flow field also affects cluster morphology and compactness. In particular, aggregates at Re=1.5 are made of needle-shaped crystals with a sort of low density “dendritic”, star-like structure, while clusters formed at Re=15 appear as compact structures likely made of spherical particles. This behaviour can be explained by stronger wall-particle adhesion as compared to particle-particles attractive forces and by the interplay between particle-wall and particle-particle interactions, whose frequency is an increasing function of the shear rate. So, at low Re cluster growth is faster and less dense structures are obtained since flow strength is not sufficient to separate particles once they collide and stick to each other. At higher Re, higher collision frequency and flow strength lead to denser structures through a balance between adhesion and erosion mechanisms. Further work to elucidate these issues is in progress. Finally, since cluster formation starts at the wall, the results of this work, although

obtained in a microfluidic geometry, can be applied more generally to the problem of fouling in continuous flow reactive systems.

5 Conclusions and perspectives

In this work, continuous flow microreactors have been presented as one of the main routes to realize “green” industrial processes for chemical synthesis, to investigate the mechanisms which govern solids transport in microdevices and as a valid alternative to traditional batch reactors. Indeed, one of the main problems of microreactors is surface fouling, which lead to channel clogging. Fouling, in fact, is a progressive deposit of solid material on the channel walls due to physical/chemical interactions between particles and the inner surface of the device. Fouling phenomenon is strongly affected by the particle and channel surface chemistry as well as by the fluid-dynamics of the system. A deep study of the literature on fouling has highlighted a lack of experimental analysis on fouling and clustering related to solids formed by organic reaction.

Here, an innovative experimental set-up based on microfluidic and microscopy techniques has been presented, aimed to the investigation of reaction kinetics of Buchwald-Hartwig amination and of the effect of the shear flow on cluster formation and growth inside microstructured devices.

Initially, a validation of two experimental set-up in continuous flow has been carried out by studying the effect of operating parameters the B-H reaction kinetic and by comparing the results with the ones of traditional batch reactors. First of all, a home-made microreactor has been proposed to verify the feasibility to process B-H reaction in a continuous flow system, obtaining equal or superior yield and conversion degree compared to classic batch systems. After that, the experimental set-up has been optimized to make the system more flexible in terms of number of feeds, this encouraging the numbering-up of the microreactor. The optimization process on the microreactor has been highlighted the possibility to change the traditional value used for running B-H reaction, increasing the reaction kinetics and reducing the procedure costs due to the small amount of reagents and catalyst. This approach has been helpful to develop another microfluidic device, which can reach high performances in continuous flow.

Moreover, the so-made microreactor has been used to investigate the mechanisms governing particle aggregation and reactor clogging using KBr solid particles from B-H amination. In particular, the attention has been focused on the effect of flow rate on particle aggregation and cluster morphology. To this aim, two different flow rates have been analysed ensuring laminar condition into the device and a uniform distribution of particles generated during the reaction into the tubular microreactor along microchip channel. The cluster growth has highlighted a strong influence of the flow rate on the cluster morphology by showing a more uniform cluster structure for the small Reynolds number compared to the irregular agglomerates at high Re number. In addition, the clogging time and the percentage have been evaluated and contrary to what was expected high flow rate encourage the channel clogging because the particle collision increases. This approach has been helpful to examine experimentally the fouling problem so far studied only by theoretic approach and simulation.

Future works will be oriented to the improvement of the novel microfluidic set-up, in order to evaluate the mechanisms at the basis of the fouling with major magnifications, to the definition of a mathematical model for describing clogging phenomena. In this view, the coupling of microscopy and microfluidics could be very helpful. By this way, the major process safety, the low costs and the possibility to investigate the solids handling could represent a real improvement in the use of the microreactors.

Appendix A

The aryl bromide ((R)-8-Bromo-5-methyl-1,2,3,4-tetrahydronaphthalen-2-ylamine)-(S)-1-(phenylethyl)amine called ArBr) has been obtained by mixing (*R*)-8-Bromo-5-methyl-1,2,3,4-tetrahydronaphthalen-2-yl)-(*S*)-1-(phenylethyl)amine Hydrochloride (20 g, 52.6 mmol) with H_2O (32 mL, 1.6 mL/g) and 50% NaOH (aq) (12 mL, 152.5 mmol) in a round-bottomed flask fitted with a reflux condenser and a magnetic stirrer. Toluene (100 mL, 5 mL/g) was added, and the resulting mixture has been heated to 60 °C and stirred. At first, the mixture appears to be very heterogeneous. Once the material has been dissolved, the mixture has been cooled to room temperature and the stirring has been stopped. At this point two liquid layers are present. By pouring them into a separating funnel it has been possible to remove the bottom aqueous layer. The top layer (organic) has been distilled under vacuum by using rotary evaporator in order to remove toluene and any water remaining. The latter process provided ArBr as a crystalline solid.

Appendix B

In this appendix, a home-made macro for Image Pro Plus 6.0 with comments to the code is listed.

```
Sub Area()
Dim i As Integer


For i = 1 To 1158
 ret = IpBlbCount()          ‘counts and measures the objects in
                             the active image or AOI
 ret = IpBlbRemoveHoles()    ‘eliminates counted objects that
                             are embedded within other counted
                             objects, and considers all pixels
                             encompassed by the perimeter of an
                             object as belonging to the object.
 ret = IpBlbSaveData("",     ‘saves, or appends, the current
 S_HEADER+S_Y_AXIS+S_DDE)    measurements or statistics to a
                             file or the Clipboard.
 ret = IpSeqPlay(SEQ_NEXT)   ‘plays an image sequence, or
                             displays a frame in that sequence.


Next i
End Sub
```

Bibliography

1. B. Gutmann, D. Cantillo and C. O. Kappe, *Angewandte Chemie International Edition*, 2015, **54**, 6688-6728.
2. U. Hintermair, G. Francio and W. Leitner, *Chemical Communications*, 2011, **47**, 3691-3701.
3. A. A. Lapkin and P. K. Plucinski, in *Chemical Reactions and Processes under Flow Conditions*, 2009, pp. 1-43.
4. C. Jiménez-González, P. Poechlauer, Q. B. Broxterman, B.-S. Yang, D. am Ende, J. Baird, C. Bertsch, R. E. Hannah, P. Dell'Orco and H. Noorman, *Organic Process Research & Development*, 2011, **15**, 900-911.
5. A. Stankiewicz, A. De Groot, H. Schoenmakers and H. Hanh, *Chemie Ingenieur Technik*, 2007, **79**, 1362-1362.
6. S. Marre and K. F. Jensen, *Chemical Society Reviews*, 2010, **39**, 1183-1202.
7. V. Hessel, B. Cortese and M. De Croon, *Chemical Engineering Science*, 2011, **66**, 1426-1448.
8. H. Lu, M. A. Schmidt and K. F. Jensen, *Lab on a Chip*, 2001, **1**, 22-28.
9. A. J. Parrott, R. A. Bourne, G. R. Akien, D. J. Irvine and M. Poliakoff, *Angewandte Chemie International Edition*, 2011, **50**, 3788-3792.
10. F. Zayed, L. Greiner, P. S. Schulz, A. Lapkin and W. Leitner, *Chemical Communications*, 2008, 79-81.
11. F. Castro, S. Kuhn, K. Jensen, A. Ferreira, F. Rocha, A. Vicente and J. A. Teixeira, *Chemical engineering journal*, 2013, **215**, 979-987.
12. T. Noël, J. R. Naber, R. L. Hartman, J. P. McMullen, K. F. Jensen and S. L. Buchwald, *Chemical Science*, 2011, **2**, 287-290.
13. J. S. Srai, C. Badman, M. Krumme, M. Futran and C. Johnston, *Journal of pharmaceutical sciences*, 2015, **104**, 840-849.
14. D. Kralisch and G. Kreisel, *Chemical engineering science*, 2007, **62**, 1094-1100.
15. C. Houben and A. A. Lapkin, *Current Opinion in Chemical Engineering*, 2015, **9**, 1-7.
16. A. A. Lapkin, A. Voutchkova and P. Anastas, *Chemical Engineering and Processing: Process Intensification*, 2011, **50**, 1027-1034.
17. M. Schoenitz, L. Grundemann, W. Augustin and S. Scholl, *Chemical Communications*, 2015, **51**, 8213-8228.
18. M. J. Jebrail, M. S. Bartsch and K. D. Patel, *Lab on a Chip*, 2012, **12**, 2452-2463.
19. A. Pommella, G. Tomaiuolo, A. Chartoire, S. Caserta, G. Toscano, S. P. Nolan and S. Guido, *Chemical Engineering Journal*, 2013, **223**, 578-583.
20. A. Perazzo, G. Tomaiuolo, L. Sicignano, G. Toscano, R. Meadows, S. Nolan and S. Guido, *RSC Advances*, 2015, **5**, 63786-63792.
21. S. Falß, G. Tomaiuolo, A. Perazzo, P. Hodgson, P. Yaseneva, J. Zakrzewski, S. Guido, A. Lapkin, R. Woodward and R. E. Meadows, *Organic Process Research & Development*, 2016, **20**, 558-567.
22. J. i. Yoshida, H. Kim and A. Nagaki, *ChemSusChem*, 2011, **4**, 331-340.
23. D. Russo, I. Di Somma, R. Marotta, G. Tomaiuolo, R. Andreozzi, S. Guido and A. A. Lapkin, *Organic Process Research & Development*, 2017, **21**, 357-364.
24. N. Kockmann, J. Kastner and P. Woias, *Chemical Engineering Journal*, 2008, **135**, S110-S116.
25. M. Aminian, F. Bernardi, R. Camassa, D. M. Harris and R. M. McLaughlin, *Science*, 2016, **354**, 1252-1256.
26. V. Ananthakrishnan, W. Gill and A. J. Barduhn, *AIChE Journal*, 1965, **11**, 1063-1072.
27. S. K. Bhaumik, A. Kannan and S. DasGupta, *Chemical Engineering Science*, 2015, **134**, 251-259.
28. P. Witt, S. Somasi, I. Khan, D. Blaylock, J. Newby and S. Ley, *Chemical Engineering Journal*, 2014.
29. R. L. Hartman, *Organic Process Research & Development*, 2012, **16**, 870-887.

30. D. M. Roberge, L. Ducry, N. Bieler, P. Cretton and B. Zimmermann, *Chemical engineering & technology*, 2005, **28**, 318-323.
31. D. F. Rivas and S. Kuhn, *Topics in Current Chemistry*, 2016, **374**, 1-30.
32. C. Henry, J.-P. Minier and G. Lefèvre, *Advances in colloid and interface science*, 2012, **185**, 34-76.
33. K. F. Jensen, B. J. Reizman and S. G. Newman, *Lab on a Chip*, 2014, **14**, 3206-3212.
34. K. S. Elvira, X. C. i Solvas and R. C. Wootton, *Nature chemistry*, 2013, **5**, 905-915.
35. S. Kakac, H. Liu and A. Pramuanjaroenkij, *Heat exchangers: selection, rating, and thermal design*, CRC press, 2012.
36. J. Linkhorst, T. Beckmann, D. Go, A. J. Kuehne and M. Wessling, *Scientific reports*, 2016, **6**, 22376.
37. V. J. Sieben, A. K. Tharanivasan, S. I. Andersen and F. Mostowfi, *Energy & Fuels*, 2016, **30**, 1933-1946.
38. N. Epstein, *Heat transfer engineering*, 1983, **4**, 43-56.
39. A. A. Lapkin, K. Loponov, G. Tomaiuolo and S. Guido, *Sustainable Flow Chemistry: Methods and Applications*, 2017.
40. L. Vaccaro, *Sustainable Flow Chemistry: Methods and Applications*, John Wiley & Sons, 2017.
41. S. Lazzari, L. Nicoud, B. Jaquet, M. Lattuada and M. Morbidelli, *Advances in colloid and interface science*, 2016, **235**, 1-13.
42. K. Wu and S. Kuhn, *Chim. Oggi*, 2014, **32**, 62-66.
43. B. S. Flowers and R. L. Hartman, *Challenges*, 2012, **3**, 194-211.
44. H. M. Wyss, D. L. Blair, J. F. Morris, H. A. Stone and D. A. Weitz, *Physical review E*, 2006, **74**, 061402.
45. K. Sharp and R. Adrian, *Microfluidics and Nanofluidics*, 2005, **1**, 376-380.
46. J. Marshall, *Journal of Aerosol Science*, 2007, **38**, 333-351.
47. B. Mustin and B. Stoeber, *Microfluidics and nanofluidics*, 2010, **9**, 905-913.
48. M. T. Stamm, T. Gudipaty, C. Rush, L. Jiang and Y. Zohar, *Microfluidics and nanofluidics*, 2011, **11**, 395-403.
49. G. D'Avino, M. Hulsen and P. Maffettone, *Computers & Fluids*, 2013, **86**, 45-55.
50. G. C. Agbangla, É. Climent and P. Bacchin, *Computers & Fluids*, 2014, **94**, 69-83.
51. Y. Sriphutkiat and Y. Zhou, *Sensors*, 2017, **17**, 106.
52. T. Gudipaty, M. T. Stamm, L. S. Cheung, L. Jiang and Y. Zohar, *Microfluidics and nanofluidics*, 2011, **10**, 661-669.
53. X. Xu, C. L. Ting, I. Kusaka and Z.-G. Wang, *Annual review of physical chemistry*, 2014, **65**, 449-475.
54. S. Khurshid, E. Saridakis, L. Govada and N. E. Chayen, *Nature protocols*, 2014, **9**, 1621.
55. J. Horsington, H. Lynn, L. Turnbull, D. Cheng, F. Braet, R. J. Diefenbach, C. B. Whitchurch, G. Karupiah and T. P. Newsome, *PLoS pathogens*, 2013, **9**, e1003239.
56. I. Halasz, A. Puškarić, S. A. Kimber, P. J. Beldon, A. M. Belenguer, F. Adams, V. Honkimäki, R. E. Dinnebier, B. Patel and W. Jones, *Angewandte Chemie International Edition*, 2013, **52**, 11538-11541.
57. D. W. Oxtoby, *Journal of Physics: Condensed Matter*, 1992, **4**, 7627.
58. P. S. Richard, 2007.
59. F. Mura and A. Zaccone, *Physical Review E*, 2016, **93**, 042803.
60. C. Y. Tang, T. Chong and A. G. Fane, *Advances in colloid and interface science*, 2011, **164**, 126-143.
61. L. N. S.Lazzari, B.Jaquet, M.Lattuada, M.Morbidelli, 2003.
62. J. C. Berg, *An introduction to interfaces & colloids: the bridge to nanoscience*, World Scientific, 2010.
63. A. Zaccone, H. Wu, D. Gentili and M. Morbidelli, *Physical Review E*, 2009, **80**, 051404.
64. A. Zaccone, D. Gentili, H. Wu, 吴华 and M. Morbidelli, *The Journal of chemical physics*, 2010, **132**, 134903.
65. A. Zaccone, D. Gentili, H. Wu, M. Morbidelli and E. Del Gado, *Physical review letters*, 2011, **106**, 138301.
66. M. Lattuada, A. Zaccone, H. Wu and M. Morbidelli, *Soft matter*, 2016, **12**, 5313-5324.

67. M. Vanni and A. Gastaldi, *Langmuir*, 2011, **27**, 12822-12833.
68. P. Jarvis, B. Jefferson, J. Gregory and S. A. Parsons, *Water research*, 2005, **39**, 3121-3137.
69. B. O. Conchuir and A. Zaccone, *Physical Review E*, 2013, **87**, 032310.
70. J. Ottino, P. DeRoussel, S. Hansen and D. Khakhar, *Advances in chemical engineering*, 1999, **25**, 105-204.
71. D. Xie, H. Wu, A. Zaccone, L. Braun, H. Chen and M. Morbidelli, *Soft Matter*, 2010, **6**, 2692-2698.
72. R. K. Chakraborti, K. H. Gardner, J. F. Atkinson and J. E. Van Benschoten, *Water Research*, 2003, **37**, 873-883.
73. J. j. Zhang and X. y. Li, *AIChE Journal*, 2003, **49**, 1870-1882.
74. G. Bushell, Y. Yan, D. Woodfield, J. Raper and R. Amal, *Advances in Colloid and Interface Science*, 2002, **95**, 1-50.
75. J. C. Zahnow, J. Maerz and U. Feudel, *Physica D: Nonlinear Phenomena*, 2011, **240**, 882-893.
76. C. Lee and T. A. Kramer, *Advances in colloid and interface science*, 2004, **112**, 49-57.
77. L. Ehrl, M. Soos and M. Lattuada, *The Journal of Physical Chemistry B*, 2009, **113**, 10587-10599.
78. E.-i. Negishi, *Handbook of Organopalladium Chemistry for Organic Synthesis, 2 Volume Set*, 2003.
79. J. F. Hartwig, *Palladium-Catalyzed Amination of Aryl Halides and Related Reactions*, Wiley Online Library, 2002.
80. J. F. Hartwig, *Accounts of chemical research*, 2008, **41**, 1534-1544.
81. K. L. Billingsley, K. W. Anderson and S. L. Buchwald, *Angewandte Chemie International Edition*, 2006, **45**, 3484-3488.
82. J. P. Wolfe, S. Wagaw, J.-F. Marcoux and S. L. Buchwald, *Accounts of Chemical Research*, 1998, **31**, 805-818.
83. H. Christensen, S. Kiil, K. Dam-Johansen, O. Nielsen and M. B. Sommer, *Organic process research & development*, 2006, **10**, 762-769.
84. A. S. Guram, R. A. Rennels and S. L. Buchwald, *Angewandte Chemie International Edition in English*, 1995, **34**, 1348-1350.
85. J. Louie and J. F. Hartwig, *Tetrahedron Letters*, 1995, **36**, 3609-3612.
86. D. S. Surry and S. L. Buchwald, *Chemical Science*, 2011, **2**, 27-50.
87. S. Shekhar, P. Ryberg, J. F. Hartwig, J. S. Mathew, D. G. Blackmond, E. R. Strieter and S. L. Buchwald, *Journal of the American Chemical Society*, 2006, **128**, 3584-3591.
88. R. L. Hartman, J. R. Naber, N. Zaborenko, S. L. Buchwald and K. F. Jensen, *Organic Process Research & Development*, 2010, **14**, 1347-1357.
89. B. Marmiroli, G. Grenci, F. Cacho-Nerin, B. Sartori, E. Ferrari, P. Laggner, L. Businaro and H. Amenitsch, *Lab on a Chip*, 2009, **9**, 2063-2069.
90. V. Génot, S. Desportes, C. Croushore, J.-P. Lefèvre, R. B. Pansu, J. A. Delaire and P. R. von Rohr, *Chemical Engineering Journal*, 2010, **161**, 234-239.
91. T. No, *Chem. Sci*, 2011, **2**, 7.
92. H.-J. Federsel, M. Hedberg and W. Tian, *Organic Process Research & Development*, 2008, **12**, 512-521.
93. A. Chartoire, M. Lesieur, L. Falivene, A. M. Slawin, L. Cavallo, C. S. Cazin and S. P. Nolan, *Chemistry-A European Journal*, 2012, **18**, 4517-4521.
94. M. Soos, L. Ehrl, M. u. U. Bäbler and M. Morbidelli, *Langmuir*, 2009, **26**, 10-18.

Appendix C

Publications

- A. Perazzo, G. Tomaiuolo, **L. Sicignano**, G. Toscano, R. E. Meadows, S. P. Nolan and S. Guido "A microfluidic approach for flexible and efficient operation of a cross-coupling reactive flow." RSC Advances 5.78 (2015): 63786-63792.
- **L. Sicignano**, et al. "The effect of shear flow on microreactor clogging." (under revision)

Training school

- GRICU Meeting – Padova (IT) – 7-11/09/2015

Conferences

- Smart & Green Interfaces Conference, SGIC– COST ACTION MP1106 – Athens (GR) – 4-6/05/2016
- GRICU Meeting – Anacapri (IT) – 12-14/09/2016